RSC Advances

ROYAL SOCIETY OF CHEMISTRY

PAPER

View Article Online
View Journal | View Issue

Check for updates

Cite this: *RSC Adv.*, 2025, **15**, 45081

Hazardous gas adsorption and sensing by pristine and Pd/Mo-decorated TiS_2: a first-principles study

Tasmi Akter,[a] Md. Jahirul Islam,*[b] Md. Tawabur Rahman[b] and Jahirul Islam[a]

The rapid expansion of industrial activities necessitates the development of cost-effective and highly sensitive gas sensors for the detection of hazardous gases such as NO_2, SO_2, NO, and H_2S. Two-dimensional TiS_2 has attracted considerable attention due to its tunable electronic properties and large surface area. However, its inherently weak interaction with gas molecules limits its practical sensing performance. In this study, first-principles density functional theory (DFT) calculations within the CASTEP framework are employed to systematically investigate the adsorption and sensing characteristics of pristine, palladium (Pd), and molybdenum (Mo) decorated TiS_2 monolayers. Pristine TiS_2 exhibits physisorption for SO_2, NO_2, and H_2S, with chemisorption observed only for NO. In contrast, Pd and Mo decoration (Pd/Mo/TiS_2) significantly enhance the adsorption capability of TiS_2, leading to stronger chemisorption with higher adsorption energies, shorter adsorption distances, and pronounced charge transfer. Mo/TiS_2, in particular, demonstrates strong interactions with adsorption energies ranging from −1.01 eV to −3.421 eV. Electronic structure analysis reveals that NO_2 and NO adsorption on Mo/TiS_2 induces a transition to metallic behavior, resulting in markedly enhanced conductivity and superior sensitivity (392.732 at room temperature), surpassing both pristine and Pd/TiS_2. Recovery time analysis shows that Mo/TiS_2 undergoes extremely slow desorption, with values of 5.544×10^{37} s for NO_2 and 6.8×10^{45} s for NO under ambient conditions. In contrast, Pd/TiS_2 demonstrates more practical recovery behavior, with SO_2, NO, and H_2S desorbing within 8.598×10^{-3}, 0.003, and 65.08 s, respectively. Work function analyses further confirm that Pd and Mo decoration improve charge transport efficiency and enhance sensor selectivity. These results highlight Pd/Mo-decorated TiS_2 as promising candidates for high-performance gas sensors in industrial applications.

Received 10th September 2025
Accepted 9th November 2025

DOI: 10.1039/d5ra06850a

rsc.li/rsc-advances

1. Introduction

The advancement of human civilization requires a balance between industrial progress, environmental sustainability, and protection of public health. Rapid industrialization in modern urban environments has caused severe contamination from hazardous waste, particularly toxic gases and heavy metals. Among these pollutants, nitrogen dioxide (NO_2), sulfur dioxide (SO_2), nitric oxide (NO), and hydrogen sulfide (H_2S) are considered highly dangerous due to their significant environmental and health consequences.[1–3] NO_2 is a toxic reddish-brown gas that causes respiratory inflammation and contributes to acid rain.[4] SO_2, a colorless irritant, also leads to acid rain, vegetation damage, and respiratory issues.[5,6] NO from industrial and vehicular sources contributes to smog formation, while excess levels harm lung function.[7,8] H_2S, a flammable and poisonous gas with a rotten-egg odor, poses serious occupational and respiratory hazards, even at low concentrations.[9] The design of highly sensitive, reliable, and cost-effective gas sensors has therefore become essential to mitigate these risks.

Recent studies have explored diverse sensing materials, including graphene,[10,11] phosphorene,[12,13] carbon nanotubes (CNTs),[14,15] MXenes,[16] ZnO,[17,18] CuO,[19] and two-dimensional (2D) transition metal dichalcogenides (TMDs),[20,21] due to their promising sensitivity, selectivity, and low power consumption.[22,23] 2D TMDs have recently emerged as attractive candidates for hazardous gas sensing owing to their tunable electronic properties, large surface-to-volume ratio, efficient charge transfer ability, and low power consumption.[21,24–26] In addition to gas sensing, TMDs have been widely explored for applications in energy storage,[27,28] biosensing,[29] optoelectronics,[30] and piezoelectric devices.[31] These compounds possess the general formula XY_2, where X represents a transition metal (*e.g.*, Ti, Zr, W) and Y denotes a chalcogen element such as sulfur (S) or selenium (Se). TMDs consist of a transition metal layer between two chalcogen layers, with tunable band gaps that make them suitable for sensing applications.[32] Titanium disulfide (TiS_2) is particularly noteworthy among TMDs due to its

---

[a] *Department of Materials Science and Engineering, Khulna University of Engineering & Technology, Khulna 9203, Bangladesh*

[b] *Department of Electrical and Electronic Engineering, Khulna University of Engineering & Technology, Khulna 9203, Bangladesh. E-mail: jahirul@eee.kuet.ac.bd*

excellent chemical stability, high carrier mobility, and favorable electrical and thermal conductivity.[33] It can be synthesized in diverse nanostructured forms, including nanoribbons, nanosheets, nanoflakes, and nanodiscs.[34–36] Several experimental studies have demonstrated their potential for gas sensors. Wagh *et al.* synthesized TiS_2 nanostructures *via* hydrothermal methods for NO_2 detection, reporting enhanced sensitivity at 160 °C for 600 ppm NO_2.[37] Sakhuja *et al.* fabricated TiS_2 nanoflake sensors, achieving strong responses of 395% to 4 ppm H_2S in dry air and 234% to oxygen under ambient conditions.[38] Manzoor *et al.* studied CO_2 sensing using TiS_2 nanodiscs and observed a detection limit of 5 ppm, a 60% response rate, and a rapid response time of 37 s toward 500 ppm CO_2 under ambient conditions.[39] Sharma *et al.* reported a 72% response to 200 ppm NH_3 at atmospheric pressure with commendable selectivity.[40] These findings confirm the versatility of TiS_2 for gas sensing, although studies remain limited compared to widely investigated TMDs such as MoS_2, $MoSe_2$, and WS_2. Despite its potential, pristine TiS_2 often exhibits weak interactions with certain gas molecules, which restricts its sensitivity and selectivity, restricting its broader applicability.

To overcome this limitation, surface modification strategies such as metal doping, vacancy engineering, and transition metal (TM) decoration have been widely employed. TM decoration, in particular, introduces foreign metal atoms onto the TMDs surface, generating active sites that enhance adsorption strength, promote charge transfer, and improve overall sensing performance.[41] Transition metals such as palladium (Pd) and molybdenum (Mo) are especially attractive because of their catalytic properties and strong interactions with gas molecules.[42,43] For instance, Zhu *et al.* demonstrated enhanced SO_2 adsorption on Pd- and Pt-decorated ZrS_2 monolayers using density functional theory (DFT),[44] while Vu and Pham reported improved SO_2 sensing using Ni-, Pd-, and Pt-decorated HfS_2.[45] Similarly, Dong *et al.*[46] reported that Mo-doped WSe_2 exhibited stronger adsorption toward CO_2 and N_2O than CH_4, confirming the role of transition-metal (TM) doping in enhancing TMD-based gas sensing. Huang *et al.*[47] showed that Mo_3-doped TiS_2 improves conductivity, humidity tolerance, and oxygen adsorption, while significantly strengthening CO_2 and SO_2 adsorption through strong orbital hybridization. Saleem *et al.*[48] studied the adsorption of toxic gases (CO, CO_2, H_2S, NH_3, NO, NO_2, SO, and SO_2) on pristine and Li-decorated TiS_2 monolayers using DFT calculations. It demonstrates that Li decoration transforms TiS_2 into a metallic system with enhanced adsorption energies, faster recovery times, improved charge transfer. In our previous computational study, the sensing behavior of pristine TiS_2 toward NO_2 and SO_2 was investigated using DFT.[49] The results showed that pristine TiS_2 interacts weakly with these gases *via* van der Waals forces, displaying limited adsorption strength and minor changes in electronic properties, particularly demonstrating very low sensing ability toward SO_2.

Despite these advances, no systematic DFT investigations have explored the adsorption and sensing behavior of Pd/Mo-decorated TiS_2 monolayers toward multiple industrially relevant toxic gases. This represents a critical knowledge gap in understanding the full potential of TiS_2 for high-performance gas sensing. The present study addresses this gap by investigating the adsorption and gas-sensing properties of pristine, and Pd/Mo-decorated TiS_2 monolayers toward four toxic gases of industrial importance such as NO_2, NO, SO_2, and H_2S. Using DFT within the Cambridge Serial Total Energy Package (CASTEP), key parameters including adsorption energy, adsorption distance, charge transfer, band structure, density of states, work function, conductivity, sensitivity, and recovery time are systematically analyzed. The findings are expected to provide theoretical insights into TiS_2-based sensor performance and to guide the design of practical, high-performance gas sensors for industrial applications.

2. Computational details in DFT

In this study, all first-principles calculations were performed using CASTEP[50] program based on DFT.[51] For exchange–correlation interactions, the Perdew–Burke–Ernzerhof (PBE) functional and the Generalized Gradient Approximation (GGA)[52] were employed. van der Waals forces were computed by DFT-D corrections suggested by TS (Tkatchenko–Scheffler).[53] Initially, we optimized the unit cell of TiS_2, characterized by the space group $P\bar{3}m1$. Subsequently, we bisected this unit cell along the 001 direction and enlarged it to a 3 × 3 × 1 supercell, optimizing the supercell with a 15 Å vacuum along the *Z* direction. For unit cell optimization, the cut-off energy was set to 500 eV, and the Monkhorst–Pack grid *k*-point was 6 × 6 × 1. For supercell optimizations and further calculations, a 3 × 3 × 1 Monkhorst–Pack grid *k*-point and 500 eV cut-off energy were used. The cut-off energy and *k*-point were determined through systematic convergence tests, where the total energy change was monitored with respect to increasing plane-wave cutoff energy and *k*-point density, shown in Fig. S1. The total energy became nearly constant beyond 450 eV and 3 × 3 × 1 *k*-points; thus, 500 eV and 3 × 3 × 1 were selected for subsequent calculations to ensure accuracy and efficiency. Simulations were performed using ultrasoft pseudopotentials[54] and the Broyden–Fletcher–Goldfarb–Shanno (BFGS) minimization algorithm.[55] The convergence criteria were set as follows: maximum stress of 0.10 GPa, maximum force of 0.05 eV Å^{-1}, maximum displacement of 0.002 Å, and energy tolerance of 2.0×10^{-5} eV per atom, following values commonly adopted in previous study on similar dichalcogenide systems.[56] After the optimization of the TiS_2 supercell, selected transition metals (Pd and Mo) were introduced to decorate the TiS_2 surface. The most energetically favorable decorated configurations were determined by calculating the binding energy or cohesive energy of each configuration. To check the structural stability of the optimized supercells binding energy will be calculated using the following formula:[57,58]

$$E_{\text{coh}} = \frac{[E_{\text{total}}(\text{TiS}_2/\text{TM@TiS}_2) - E(\text{TM}) - 9E(\text{Ti}) - 18E(\text{S})]}{N} \quad (1)$$

Here, E_{coh}, $E_{\text{total}}(\text{TiS}_2/\text{TM@TiS}_2)$, $E(\text{Ti})$, $E(\text{S})$ represents the cohesive energy of TiS_2 or transition metal (TM) decorated TiS_2, total energy of TiS_2 or transition metal decorated TiS_2, the energy of isolated transition metal, the energy of isolated Ti, and the energy of isolated S, respectively.

Besides optimization of supercells, each gas molecule was built and optimized. Then, optimized gas molecules were adsorbed on the supercell's surface. After gas adsorption, the structures of the gas-adsorbed systems were further optimized. The adsorption energy of the gas molecules on the monolayer was calculated using the following equation:[59]

$$E_{\text{ads}} = E_{\text{total}} - (E_{\text{substrate}} + E_{\text{gas}}) \tag{2}$$

Here, E_{ads}, E_{total}, $E_{\text{substrate}}$, and E_{gas} represent the adsorption energy of gas molecules, the total energy of systems after gas adsorption, the total energy of systems before gas adsorption, and the total energy of the isolated gas molecule, respectively.

Charge transfer (ΔQ) was calculated *via* the Hirshfeld charge analysis method to ascertain the adsorption capacity, with the corresponding calculation formula presented below:[60,61]

$$\Delta Q = Q_{\text{after}} - Q_{\text{before}} \tag{3}$$

In this context, ΔQ, Q_{after}, and Q_{before} represent the charge transfer between the gas and the monolayer, the charge of the gas molecules after it has been adsorbed, and the charge of the isolated gas before it has been adsorbed, respectively. Charge density differential maps (CDD) were produced to visualize charge accumulation and depletion surrounding the gas molecules and monolayer surface.

Electronic properties were computed using the spin-polarized GGA-PBE functional with a cutoff energy of 500 eV and a 3 × 3 × 1 Monkhorst–Pack *k*-point grid, consistent with the geometry optimization setup. Alterations in electronic characteristics during gas adsorption will facilitate the analysis of the sensor's behavior. For this purpose, electronic band structures, as well as partial (PDOS) and total (TDOS) density of states, were calculated for all systems before and after gas adsorption. The conductivity of any substance is related to its band gap. The conductivity of the adsorbent, both prior to and after gas adsorption, is determined using the following equation:[62]

$$\sigma = A\exp\left(\frac{-E_{\text{g}}}{2KT}\right) \tag{4}$$

In this expression, A denotes a constant, E_{g} refers to the band gap, K is the Boltzmann constant, and T represents the absolute temperature in Kelvin.

Sensitivity (S) is a key parameter used to assess the effectiveness of materials in gas sensing applications. A higher sensitivity signifies stronger gas–material interactions, indicating improved adsorption and surface activity. Evaluating sensitivity is therefore essential to determine how effectively pristine and decorated TiS_2 monolayers respond to different gases, which directly influences their gas-sensing performance. The sensitivity of an adsorbent toward specific gas molecules was evaluated by monitoring changes in their electrical conductivity upon gas exposure, typically expressed as the difference in conductivity with and without the presence of the gas.[63]

$$S = \left(\left|\frac{\sigma_{\text{pure}} - \sigma_{\text{substrate+gas}}}{\sigma_{\text{pure}}}\right|\right) \tag{5}$$

σ_{pure}, and $\sigma_{\text{substrate+gas}}$ represent the conductivity of the adsorbent before gas adsorption and after adsorption, respectively. Selectivity was calculated using the following formula:[64]

$$K = \frac{S_{\text{target}}}{S_{\text{intereferent}}} \tag{6}$$

Here, K represents selectivity, S_{target} is the sensitivity of highest sensitive gas towards a specific system and $S_{\text{intereferent}}$ is the other interfering gases.

Recovery time refers to the period required for a material to restore its initial conductivity after being exposed to a gas.[65] A shorter recovery time indicates quicker desorption of gas molecules from the material's surface.[66] Sensor recovery time was calculated using the van't-Hoff–Arrhenius equation:[67]

$$\tau = \frac{1}{f}\exp\left(\frac{-E_{\text{ad}}}{KT}\right) \tag{7}$$

Here, K, T, E_{ad}, and f represent Boltzmann's constant, the absolute temperature, adsorption energy, and the frequency of UV radiation (ranging from 10^{12} to 3×10^{14} Hz), respectively.

The minimum energy required to excite an electron from inside a solid to the vacuum level, where it becomes free to escape the material, is known as the work function (WF). The WF is strongly influenced by the surface properties of a material. Any modification at the surface can alter the WF, which in turn affects how easily electrons can escape. In the field of photovoltaics, the WF plays a vital role in determining a material's electrical conductivity and chemical reactivity.[68,69] Gas adsorption leads to a pronounced change in the work function (ϕ), which can be exploited for developing work function-based sensors. These variations in ϕ can be experimentally measured using the Kelvin probe method, providing a practical route for sensor fabrication.[70] The work function (ϕ) is defined by the difference between the vacuum electrostatic potential (E_{vacuum}) and the Fermi level (E_{Fermi}):[71]

$$\phi = E_{\text{vacuum}} - E_{\text{Fermi}} \tag{8}$$

3. Results and discussion

3.1 Structural analysis of pristine TiS_2 and Pd/Mo decorated TiS_2

Before the adsorption of gas molecules on monolayer surfaces, all gases and the adsorbents (where gas molecules are adsorbed) should be optimized. The selected gas molecules' geometries, including NO_2, SO_2, NO, and H_2S, were optimized using the CASTEP module. The optimized gas molecule structures are shown in Fig. 1. The bond lengths and angles of optimized gases are listed in Table 1. Bond lengths of NO_2, SO_2, NO, and H_2S are 1.230, 1.195, 1.448, and 1.350 Å, respectively. These values are close enough to the previous findings.[45,66,72] The optimized 3 × 3 × 1 supercell of pristine TiS_2, most stable Pd-decorated TiS_2 (Pd/TiS_2), and Mo-decorated TiS_2 (Mo/TiS_2) are

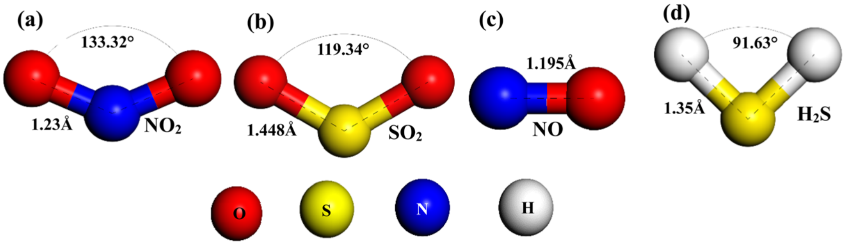

Fig. 1 Optimized gas molecule structures (a) NO_2, (b) SO_2, (c) NO, and (d) H_2S.

Table 1 Bond lengths and angles of optimized monolayers and gas molecules

	Bond lengths before gas adsorption (Å)						Bond lengths after gas adsorption (Å)				
							Ti–S				
Compounds	Ti–S	Pd–Ti	Mo–Ti	N–O	S=O	H–S	NO_2	SO_2	NO	H_2S	Angles (°)
TiS_2	2.433	—	—	—	—	—	2.431	2.433	2.406	2.428	89.52 (Ti–S–Ti)
Pd/TiS_2	2.504	2.294, 2.292	—	—	—	—	2.487	2.457	2.530	2.483	111.62 (S–Pd–S)
Mo/TiS_2	2.514	—	2.248, 2.250	—	—	—	2.535	2.518	2.562	2.515	111.83 (S–Mo–S)
NO_2	—	—	—	1.230	—	—	—				133.32 (O–N–O)
SO_2	—	—	—	—	1.448	—	—				119.34 (O–S–O)
NO	—	—	—	1.195	—	—	—				180 (N–O)
H_2S	—	—	—	—	—	1.350	—				91.63 (H–S–H)

shown in Fig. 2(a), (b) and (c), respectively. The lattice parameters of optimized pristine TiS_2 are $a = b = 3.414$ Å, which is very close to previously documented values, previous experimental value is 3.3976 Å (ref. 73) and computational value is 3.407 Å.[74] The optimized pristine TiS_2 is thermodynamically stable as the calculated cohesive energy using eqn (1) is negative (−6.48 eV per atom). The Ti–S bond length of pristine TiS_2 is 2.433 Å, in the case of Pd/TiS_2, this bond length increases to 2.504 Å, and for Mo/TiS_2, the Ti–S bond length is 2.514 Å. The increase in bond length may arise from the interaction of the decorated atoms with TiS_2, which have diverse sizes and charge distributions. The trend in Ti–S bond length is $TiS_2 < Pd/TiS_2 < Mo/TiS_2$. Here, the greater bond elongation in Mo/TiS_2 reflects more enhanced electronic interaction, higher degree of charge delocalization between the Mo atom and the TiS_2 layer, which in turn increases the availability of active sites for gas adsorption. Therefore, it serves as an indicator of increased surface reactivity arising from electronic modulation which may lead to stronger adsorption energies in case of Mo/TiS_2. The Ti–S–Ti bond angle is 89.52° for pristine TiS_2, S–Pd–S, and S–Mo–S bond angles are 111.62° and 111.83°, respectively.

One of the principal concerns was the geometric stability subsequent to the Pd and Mo decoration in the pristine TiS_2 layer. For this purpose, three positions on the TiS_2 layer were selected, illustrated in Fig. 2(a), where Pd and Mo atoms were decorated: above the Ti atom, above the S atom, and above the hollow site. Upon complete geometry optimization of the structure, the binding energies at these three places are computed using eqn (1) to ascertain the most stable configuration of the $Pd/Mo/TiS_2$ monolayer. The more negative binding energy indicates the favorable stable systems. In case of Pd/TiS_2, the computed binding energies for these locations are −6.37, −6.33, and −6.38, respectively and for Mo/TiS_2, the binding energies are −6.59, −6.6096, −6.6099 eV, respectively. The maximum binding energy, found at the hollow site (−6.38 eV for Pd/TiS_2) and (−6.6099 eV for Mo/TiS_2), indicates that the hollow site is the most stable for both Pd/TiS_2 and Mo/TiS_2 monolayers. These stable structures are shown in Fig. 2(b) and (c), where Pd and Mo create covalent bonds with surrounding S atoms. The Pd–S and Mo–S connections have an average bond length of 2.293 Å and 2.249 Å, respectively, which are less than the total of the atomic covalent radii of S (1.04 Å) + Pd (1.39 Å) and S (1.04 Å) + Mo (1.54 Å),[75] suggesting a substantial covalent nature and a strong metal–sulfur interaction. The Pd and Mo atoms appear to be firmly anchored in the hollow site, the most energetically advantageous configurations for the Pd/TiS_2 and Mo/TiS_2 monolayers, based on strong covalent bonds. Further calculations of gas adsorptions were conducted on these most stable structures. Additionally, to confirm that the pristine and Pd/Mo-decorated TiS_2 structures are stable at high temperatures, we performed *ab initio* molecular dynamics (AIMD) simulations at 398 K with a 1 fs time step for a total simulation period of 5 ps. As shown in Fig. S2, the total energy of each system (Figs. S2(a), (c) and (e)) fluctuates slightly around a constant mean value throughout the simulation period, indicating the absence of any structural distortion or bond breaking. Correspondingly, the temperature profiles (Fig. S2(b), (d) and (f)) remain stable around the target value, showing only minor fluctuations typical of thermal equilibrium conditions. These observations confirm that the TiS_2, Pd/TiS_2, and Mo/TiS_2

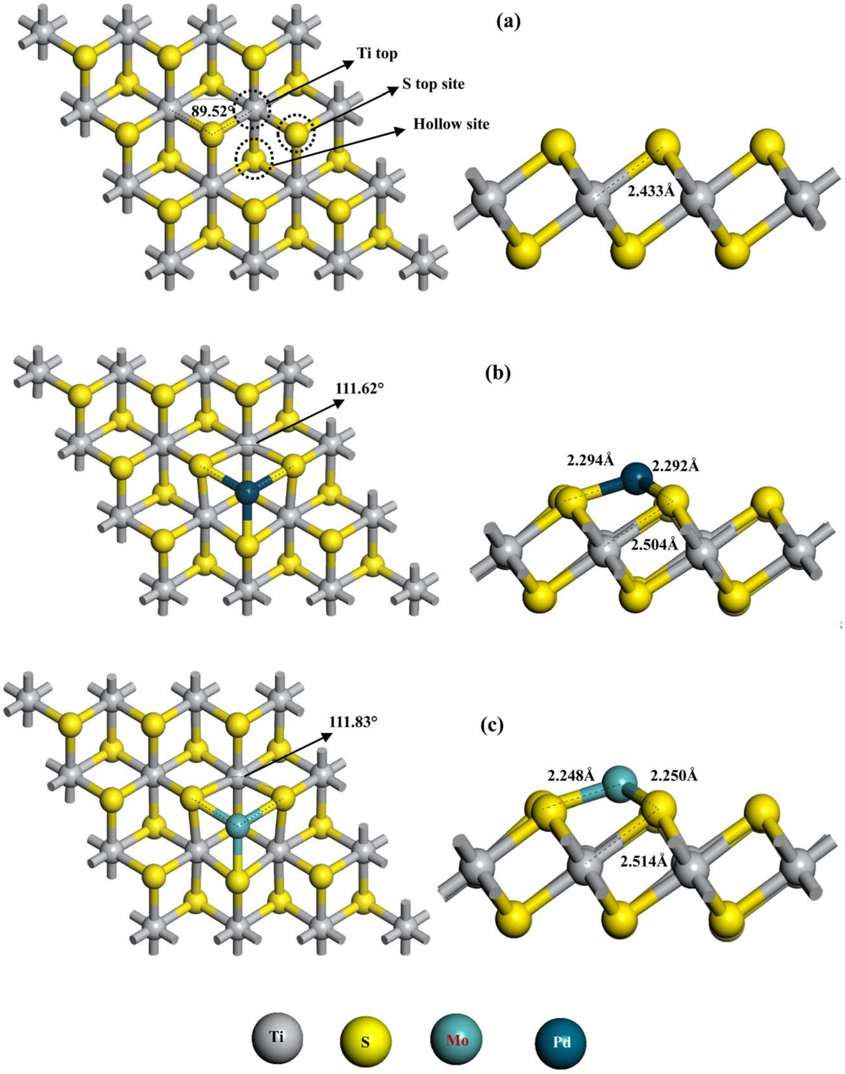

Fig. 2 (a) Optimized TiS_2 monolayer showing three possible decoration sites, (b and c) most energetically favorable Pd-decorated TiS_2 and Mo-decorated TiS_2 monolayers, respectively.

monolayers maintain their structural integrity at elevated temperatures, demonstrating their excellent dynamic and thermal stability, which is essential for reliable sensing performance under practical operating conditions.

3.2 Gas adsorption properties on pristine and Pd/Mo decorated TiS_2

After the geometry optimization of the TiS_2 monolayer, NO and H_2S gas molecules are adsorbed on the TiS_2 monolayer surface in different positions. Adsorbed systems are then optimized, and the most stable systems are identified based on the minimum adsorption energy.[76] These most stable systems are shown in Fig. 3. The calculated adsorption characteristics, for instance, adsorption energy (E_{ads}), adsorption distance (D), charge transfer (ΔQ), changes in bond length of gas molecules (L_g), and band gap (E_g) are listed in Table 2. The adsorption energy is calculated using eqn (2). The minimum adsorption energies for NO and H_2S on pristine TiS_2 are -0.188 eV and -0.602 eV, respectively. Additionally, the minimum adsorption distances between the gas molecules and TiS_2 monolayer are 2.114 Å for NO and 3.321 Å for H_2S. The adsorption energy and distance both suggest that NO adsorption on TiS_2 is chemisorption. In the case of H_2S gas, the adsorption energy is low and the adsorption distance is much greater than the sum of the covalent radii of H and S.[75] The connection between the sulfur atom of TiS_2 and the hydrogen atom in H_2S occurs through weak van der Waals bonds, and this sort of adsorption is classified as physisorption.[60] Significant alterations in bond lengths of the adsorbed gas molecules are seen upon adsorption, as illustrated in Table 2. The N–O bond in NO is shortened by 0.001 Å, and the H–S bond in H_2S is elongated by 0.001 Å. The alteration in bond length of gas molecules during gas adsorption indicates the interaction between the gas molecules and the TiS_2 monolayer surface. For getting more insights into interactions between gas molecules and TiS_2 monolayer, charge transfer due to gas adsorption is calculated using eqn (3),

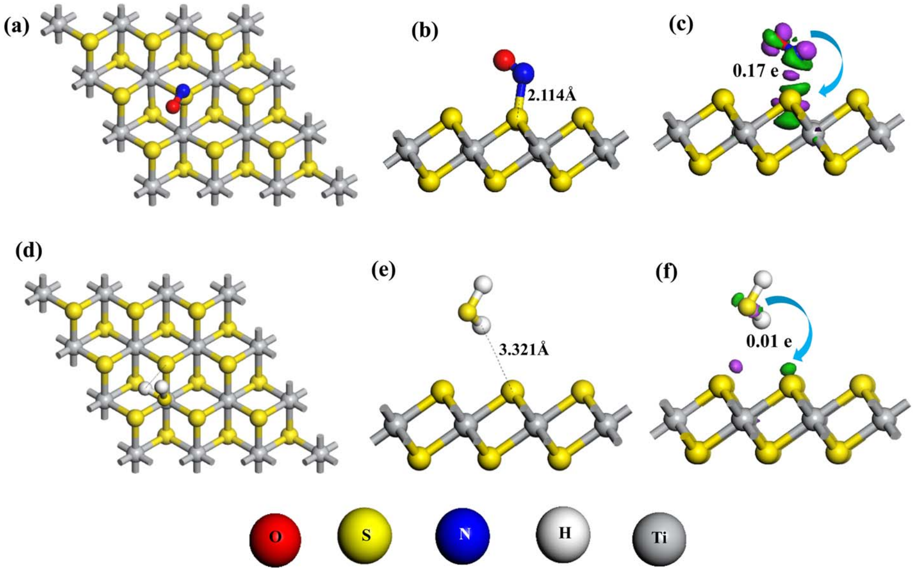

Fig. 3 Most stable optimized systems of adsorbed gas molecules on TiS_2 monolayer: (a and b) top and side views of NO@TiS_2; (d and e) top and side views of H_2S@TiS_2; and (c and f) the corresponding charge density difference (CDD) of NO@TiS_2 and H_2S@TiS_2.

Table 2 Computed adsorption properties, adsorption energy (E_{ads}), charge transfer (ΔQ), adsorption distance (D), bond length (L_g) of gas molecules after adsorption, band gap (E_g)

Compound	Gas	E_{ads} (eV)	ΔQ (e)	D (Å)	L_g (Å)	E_g (eV)
TiS_2	—	—	—	—	—	0.098
	NO_2 (ref. 49)	−0.204	−0.06	3.608	1.234	0
	SO_2 (ref. 49)	−0.235	−0.01	3.684	1.449	0.099
	NO	−0.602	0.17	2.114	1.194	0
	H_2S	−0.188	0.01	3.321	1.351	0.103
Pd/TiS_2	—	—	—	—	—	0.079
	NO_2	−0.979	−0.21	2.130	1.248	0
	SO_2	−0.588	−0.09	2.343	1.450	0.144
	NO	−1.455	0.07	1.887	1.196	0
	H_2S	−0.817	0.16	2.489	1.355	0.182
Mo/TiS_2	—	—	—	—	—	0.307
	NO_2	−2.942	−0.22	2.018	1.386	0
	SO_2	−1.01	−0.1	2.345	1.456	0.351
	NO	−3.421	−0.17	1.795	1.219	0
	H_2S	−1.312	0.17	2.544	1.408	0.398

employing Hirshfeld charge distributions for both gases and monolayers. NO and H_2S both act as electron donors; here, NO transfers 0.17 electrons and H_2S transfers 0.01 electrons to the TiS_2 monolayer. These findings also suggest that the interaction between NO and the TiS_2 monolayer is a strong chemisorption, whereas H_2S shows a weak physical interaction. Furthermore, we have examined the charge density difference map (CDD) to visualize charge accumulation and depletion surrounding the gas molecules and the TiS_2 surface. The CDD of NO@TiS_2 and H_2S@TiS_2 are shown in Fig. 3(c) and (f), where purple color indicates charge accumulation and green color denotes charge depletion. There is significant charge accumulation and depletion between the N–S bond in NO@TiS_2; in contrast, between H from H_2S and S from TiS_2, we found very little charge distribution. In our previous study, we investigated the adsorption characteristics of NO_2 and SO_2 on the pristine TiS_2 monolayer. For comparing their adsorption characteristics with NO@TiS_2 and H_2S@TiS_2, we have added the adsorption properties in Table 2. While comparing these four gas molecules' adsorptions on TiS_2, only NO shows chemisorption, and the other three gases (NO_2, SO_2, and H_2S) show weak physical interactions.

After completing structural relaxation, Fig. 4 illustrates the lowest energy adsorption configurations for the Pd/TiS_2 and Mo/TiS_2 monolayers interacting with four gas molecules, including NO_2, SO_2, NO, and H_2S. The adsorption characteristics for these gas molecules on the Pd/TiS_2 and Mo/TiS_2 monolayers are presented in Table 2. The adsorption energies for NO_2, SO_2, NO, and H_2S on Pd/TiS_2 are −0.979, −0.588, −1.455, and −0.817 eV, respectively, suggesting that these gases and the Pd/TiS_2 surface have a substantial interaction. The observation is additionally supported by the adsorption structures illustrated in Fig. 4(a)–(d) and the adsorption distances presented in Table 2, indicating the formation of Pd–N, Pd–S, Pd–N, and Pd–H chemical bonds in adsorbed systems. This suggests the chemisorption-type adsorption behavior for all gas molecules on the Pd/TiS_2 monolayer. The adsorption strength of these gases on the Pd/TiS_2 surface adheres to the following hierarchy: NO > NO_2 > H_2S > SO_2. This pattern indicates that the surface interactions with NO are the most robust, perhaps due to the establishment of strong Pd–N bonds, whereas SO_2 demonstrates relatively weaker interactions compared to other gases. Although SO_2 shows relatively weaker interactions, its adsorption energy notably increases upon Pd decoration compared to pristine TiS_2. Upon adsorption on the Pd/TiS_2 monolayer, noticeable alterations in the bond lengths of the adsorbed gas molecules are observed, as summarized in Table 2. Specifically, the N–O bond in NO_2, one of the S–O bonds in

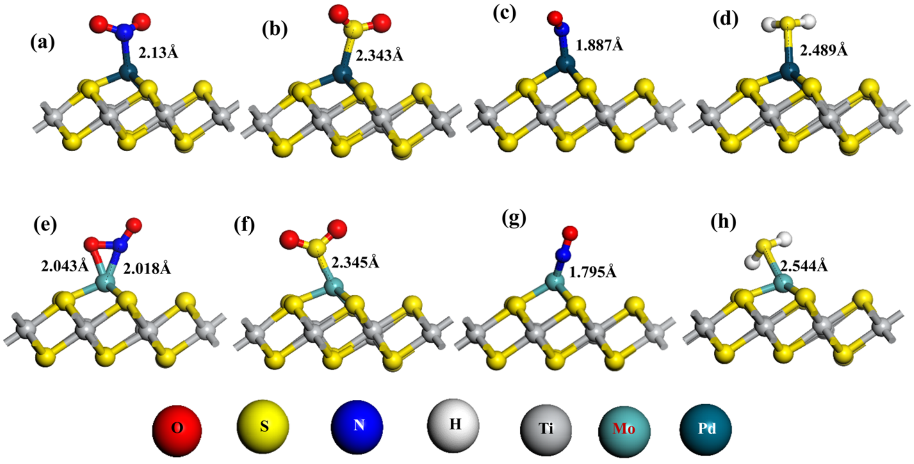

Fig. 4 Most stable optimized systems of adsorbed gas molecules on decorated-TiS_2 monolayers: (a) NO_2@Pd/TiS_2, (b) SO_2@Pd/TiS_2, (c) NO@Pd/TiS_2, (d) H_2S@Pd/TiS_2, (e) NO_2@Mo/TiS_2, (f) SO_2@Mo/TiS_2, (g) NO@Mo/TiS_2, and (h) H_2S@Mo/TiS_2.

SO_2, the N–O bond in NO, and one of the H–S bonds exhibit elongations of 0.018 Å, 0.002 Å, 0.001 Å, and 0.005 Å, respectively. These variations in bond lengths suggest different strengths and natures of interactions between the gas molecules and the Pd/TiS_2 surface. Hersfield charge transfer analysis further indicates that NO and H_2S act as electron donors, transferring approximately 0.07 and 0.16 electrons, respectively, to the Pd/TiS_2 monolayer. Conversely, NO_2 and SO_2 function as electron acceptors, receiving about 0.21 and 0.09 electrons, respectively, from the substrate. Additionally, charge density difference (CDD) plots (Fig. 5) illustrate significant charge redistribution, including both accumulation and depletion, primarily around the Pd–X bonds (X = N, S, O) formed during adsorption. This charge reorganization, along with evidence for orbital overlapping, indicates strong interaction between the gases and the Pd site. Overall, the combination of adsorption energies, adsorption distance, charge transfer values, and CDD analysis confirms that the interactions between NO, NO_2, SO_2, H_2S, and the Pd/TiS_2 monolayer are predominantly chemical in nature, involving substantial electron exchange.

In the case of the Mo-decorated TiS_2 monolayer, adsorption energies for NO_2, SO_2, NO, and H_2S were calculated to be −2.942, −1.01, −3.421, and −1.312 eV, respectively. These values reflect a strong interaction between the gas molecules and the modified surface, which are significantly larger than pristine TiS_2 and Pd-decorated TiS_2. These suggest the strong chemisorption of these gas molecules on the Mo/TiS_2 surface. Their adsorption distances tabulated in Table 2 and Fig. 4(e)–(h) also imply the strong covalent bonding between the gas molecules and the Mo atom of the substrate. This interaction also induces noticeable changes in the molecular structures of the adsorbed species. For NO_2, SO_2, NO, and H_2S, the bond lengths are elongated by 0.156, 0.008, 0.024, and 0.58 Å, respectively, compared to their isolated forms. The bond length change is also more prominent for Mo/TiS_2 compared to pristine and Pd/TiS_2. The change in Ti–S bond length is also observed in all three systems after gas adsorption. Though the change is less in

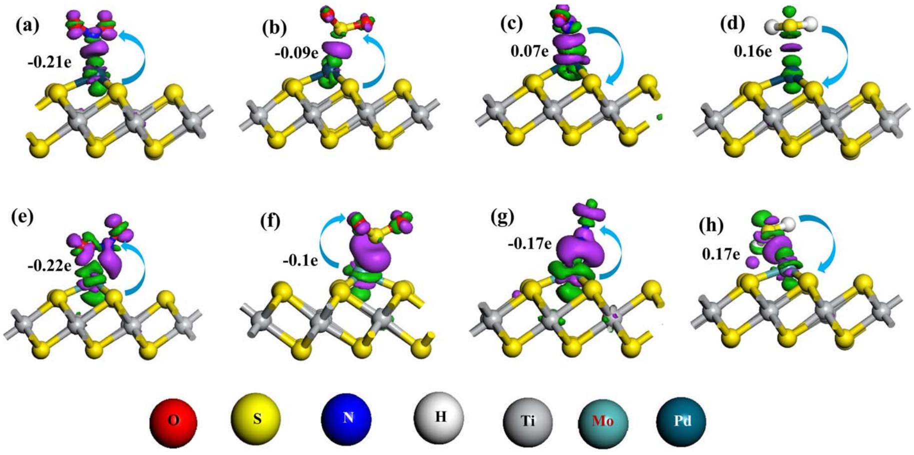

Fig. 5 Charge density difference (CDD) mapping of gas adsorbed systems: (a) NO_2@Pd/TiS_2, (b) SO_2@Pd/TiS_2, (c) NO@Pd/TiS_2, (d) H_2S@Pd/TiS_2, (e) NO_2@Mo/TiS_2, (f) SO_2@Mo/TiS_2, (g) NO@Mo/TiS_2, and (h) H_2S@Mo/TiS_2. Here, purple and green colors denote charge accumulation and depletion, respectively.

pristine TiS_2 compared to decorated TiS_2. Ti–S bond length changes after gas adsorption are depicted in Table 1. For pristine TiS_2, Ti–S bond lengths changes are 0.002 and 0.00 for NO_2 and SO_2 gases, these little changes also matched with their weak physical interaction characteristics whereas in case of NO, Ti–S bond length changes more indicating strong interaction of NO with TiS_2. For both decorated systems significant changes in Ti–S bond length can match their strong chemical interactions.

Further insights were obtained from Hirshfeld charge transfer analysis, which indicates that H_2S acts as an electron donor, transferring 0.17 electrons to the Mo/TiS_2 surface. Conversely, NO_2 and SO_2, and H_2S act as electron acceptors, gaining 0.22, 0.1, and 0.17 electrons, respectively, from the substrate. These results are consistent with the charge density difference (CDD) plots shown in Fig. 5, which reveal significant electron accumulation and depletion around the Mo–X (X = N, O, S) bonding regions. This charge redistribution confirms strong orbital hybridization and underlines the chemical nature of the interaction.

Overall, these findings suggest that Mo-functionalized TiS_2 is a more promising candidate for detecting these toxic gases than pristine and Pd/TiS_2 monolayers based on adsorption characteristics. The interaction strength of the gases with the monolayers decreases in the following order: Mo/TiS_2 > Pd/TiS_2 > pristine TiS_2. Such comparative analysis provides valuable guidance for the rational design of selective and efficient gas sensors based on the transition of metal-decorated 2D materials.

3.3 Electronic properties of pristine/Pd/Mo TiS_2 before and after gas adsorption

To investigate how gas molecules interact with the pristine and Pd/Mo-decorated TiS_2 monolayers and influence their electronic characteristics and thus their conductivity, the band structures of the adsorption systems were examined. This analysis illustrates the modifications in the electronic response of the monolayer upon gas adsorption, offering valuable insights for enhancing gas-sensing efficiency. Fig. 6 depicts the band structures of pristine TiS_2, Pd/TiS_2, and Mo/TiS_2 before gas adsorption and the band structures of adsorbed systems (NO@TiS_2 and H_2S@TiS_2). Here, band structures are shown for only the spin-up state, as the band structures for both spin states are similar. The bandgap of the pristine TiS_2 monolayer is found to be 0.098 eV (indirect) using the GGA-PBE functional, which is close to previous literature (0.112 eV).[74] Pd-decoration and Mo-decoration tune the band gap of TiS_2 to 0.079 eV (indirect) and 0.307 eV (direct), respectively.

Here band gap change is more pronounced for Mo/TiS_2 than for Pd/TiS_2. These serve as reference points for assessing the impact of adsorbates on the electronic properties of the systems. As shown in Fig. 6(d) and (e), the adsorption of NO on TiS_2 reduces the band gap of TiS_2 to 0 eV, which is metallic, and H_2S increases the band gap of pristine TiS_2 slightly (0.103 eV). Band gap results listed in Table 2 from our previous study[49] depict that NO_2 adsorption makes NO_2@TiS_2 again metallic, and SO_2 increases the band gap very little (0.099 eV). Conductivity and sensitivity are directly influenced by the band gap. Upon gas adsorption, an increase in the band gap leads to reduced conductivity, while a decrease in the band gap results in enhanced conductivity. The conductivity results for different adsorption systems at three different temperatures (298, 358, and 398 K) are listed in Table 3. The conductivity increases for NO_2 and NO from 0.149 to 1.00 A per ohm per m, whereas for SO_2 and H_2S conductivity decreases very little (0.149 to 0.146 A

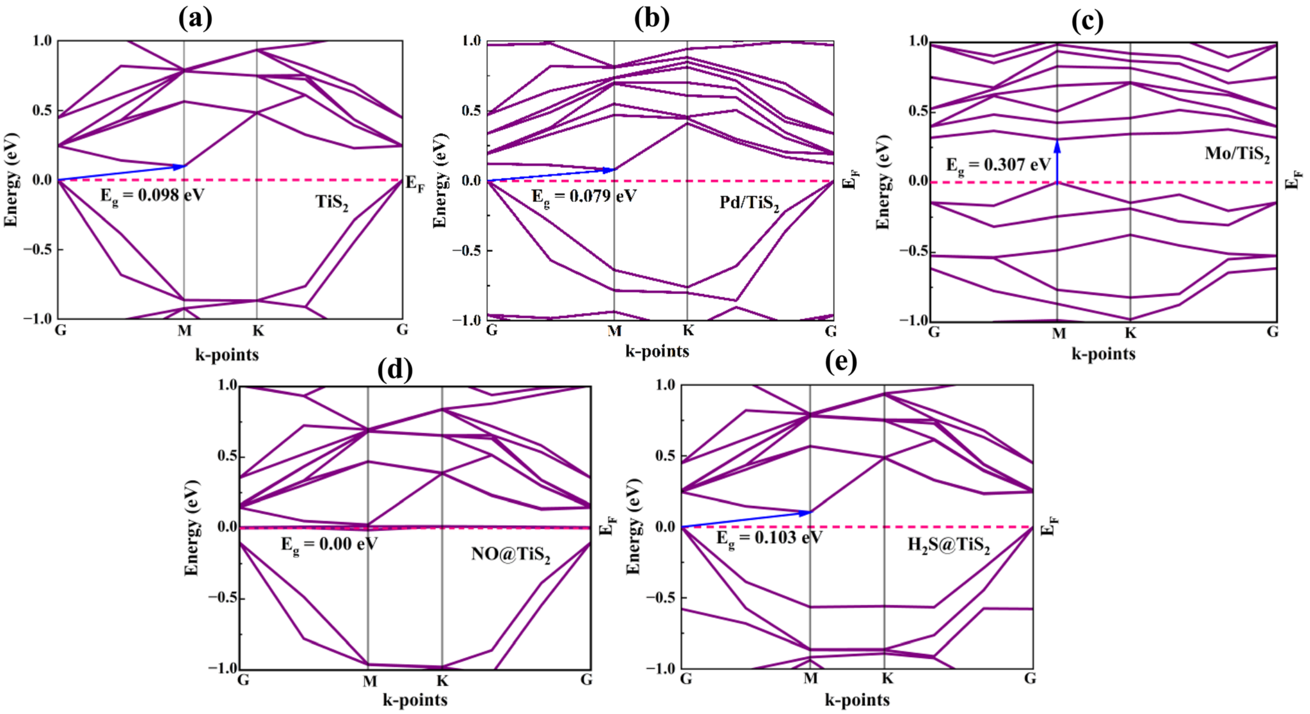

Fig. 6 Electronic band structures (a) pristine TiS_2, (b) Pd/TiS_2, (c) Mo/TiS_2, (d) NO@TiS_2, and (e) H_2S@TiS_2.

Table 3 Conductivity (σ), sensitivity (S) of gas adsorption systems at three different temperatures (298 K, 358 K, and 398 K), and selectivity (K) at 298 K

System	σ (A per ohm per m) $K = 298$ K	σ (A per ohm per m) $T = 358$ K	σ (A per ohm per m) $T = 398$ K	S ($T = 298$ K)	S ($T = 358$ K)	S ($T = 398$ K)	K ($T = 298$ K)
TiS_2	0.149	0.204	0.2397	—	—	—	—
$NO_2@TiS_2$	1.00	1.00	1.00	5.737	3.893	3.171	1.00
$SO_2@TiS_2$	0.146	0.201	0.236	0.019	0.016	0.015	301.95
$NO@TiS_2$	1.00	1.00	1.00	5.737	3.893	3.171	1.00
$H_2S@TiS_2$	0.135	0.189	0.223	0.093	0.078	0.070	61.688
Pd/TiS_2	0.215	0.279	0.317	—	—	—	—
$NO_2@Pd/TiS_2$	1.00	1.00	1.00	3.645	2.591	2.158	1.00
$SO_2@Pd/TiS_2$	0.061	0.097	0.123	0.719	0.652	0.613	5.07
$NO@Pd/TiS_2$	1.00	1.00	1.00	3.645	2.591	2.158	1.00
$H_2S@Pd/TiS_2$	0.013	0.026	0.038	0.942	0.906	0.881	3.87
Mo/TiS_2	0.003	0.007	0.012	—	—	—	—
$NO_2@Mo/TiS_2$	1.00	1.00	1.00	392.723	143.625	86.727	1.00
$SO_2@Mo/TiS_2$	0.002	0.004	0.007	0.576	0.51	0.474	681.81
$NO@Mo/TiS_2$	1.00	1.00	1.00	392.723	143.625	86.727	1.00
$H_2S@Mo/TiS_2$	0.001	0.002	0.004	0.83	0.772	0.735	473.16

per ohm per m for SO_2 and 0.135 A per ohm per m for H_2S). Electronic band structures of gas adsorbed systems on Pd/TiS_2 and Mo/TiS_2 are shown in Fig. 7. In the case of Pd/TiS_2, the corresponding bandgap values are 0.00 eV for NO and NO_2, 0.144 eV for SO_2, and 0.182 eV for H_2S. In the case of NO_2 and NO, adsorption systems again exhibit metallic nature, thus increasing the conductivity. For SO_2 and H_2S, the conductivity decreases significantly. When it comes to Mo/TiS_2, the band gap undergoes remarkable shifts after the adsorption of gas species. After adsorption, the band gap narrows dramatically to 0 eV from 0.307 eV for NO_2 and NO, indicating a transition toward metallic character and pointing to a significant rise in electrical conductivity (0.003 to 1.00 A per ohm per m). This pronounced effect indicates that NO_2 and NO exert the strongest influence on the electronic behavior of Mo/TiS_2 compared to the other studied gases. SO_2 and H_2S adsorption result in band gaps of 0.351 eV and 0.398 eV, respectively, both larger than the band gap of Mo/TiS_2, suggesting diminished conductivity relative to the Mo/TiS_2 monolayer surface.

The comparative analysis of band structures demonstrates that adsorption of NO_2 and NO markedly reduces the band gap of TiS_2-based systems to metallic states, thereby enhancing their conductivity, while SO_2 and H_2S interactions induce only slight band gap increases associated with reduced conductivity. Notably, Mo/TiS_2 exhibits the most substantial electronic modulation among the studied monolayers, underscoring its strong potential as a highly sensitive and selective candidate for gas-sensing applications.

In order to gain deeper insights into the influence of adsorbed molecules on the electronic structure of the substrate, a density of states (DOS) analysis was conducted. The outcomes for the pristine TiS_2, Pd/TiS_2, and Mo/TiS_2 adsorption systems are illustrated in Fig. 8. The total density of states (TDOS) and partial density of states (PDOS) for pristine TiS_2 and Pd/TiS_2 are presented in Fig. 8(a). The TDOS curves reveal that decorating with Pd induces notable modifications in the electronic structure, Pd/TiS_2 exhibiting additional states near the Fermi level (E_F). The PDOS analysis further elucidates the contributions of specific atomic orbitals: Ti-3d states dominate near E_F, while S-3p states are spread across a broader energy range. Notably, the Pd-4d state contributes significantly near the Fermi level in Pd/TiS_2, suggesting that Pd incorporation introduces new electronic states primarily derived from Pd orbitals. Fig. 8(b) shows the TDOS and PDOS for pristine TiS_2 and Mo/TiS_2. Mo decoration introduces states near the Fermi level. The PDOS indicates that additional Mo-4d contributions appear and hybridize with Ti-3d states, leading to a redistribution of states around E_F. These electronic modifications suggest that decoration may facilitate faster charge transfer with adsorbed gas molecules and improve TiS_2's sensitivity and performance in gas sensors.

The TDOS for NO adsorption on TiS_2 shown in Fig. 8(c) reveals a clear modification of the DOS near the Fermi level compared to pristine TiS_2, indicating a strong interaction between NO molecules and the TiS_2 surface. The PDOS confirms that the newly introduced states originate mainly from the N-2p and O-2p orbitals, which overlap with Ti-3d states near E_F. This orbital hybridization facilitates efficient charge transfer, suggesting a chemisorption-type interaction. In contrast, H_2S adsorption causes relatively weaker changes in the DOS distribution around E_F. The contributions from H-1s and S2-3p (S from H_2S) orbitals are small and show limited overlap with Ti-3d states, indicating a weaker electronic coupling compared to NO adsorption. This implies that the interaction of H_2S with TiS_2 is more physisorptive in nature, with lower charge transfer efficiency. These analyses are also inconsistent with the Hersfield charge analysis. In the case of NO_2 adsorption on Pd/TiS_2, substantial perturbation of the TDOS occurs around the Fermi level, driven mainly by the hybridization of N-2p/O-2p states with Pd-4d orbitals. This demonstrates strong chemisorption with considerable charge transfer. For SO_2 adsorption on Pd/TiS_2, the TDOS shows a clear modification near the Fermi level compared to pristine Pd/TiS_2, indicating strong orbital hybridization. The PDOS reveals hybridization of Pd-4d, Ti-3d, with S2-3p and O-2p (from SO_2), confirming charge transfer and orbital

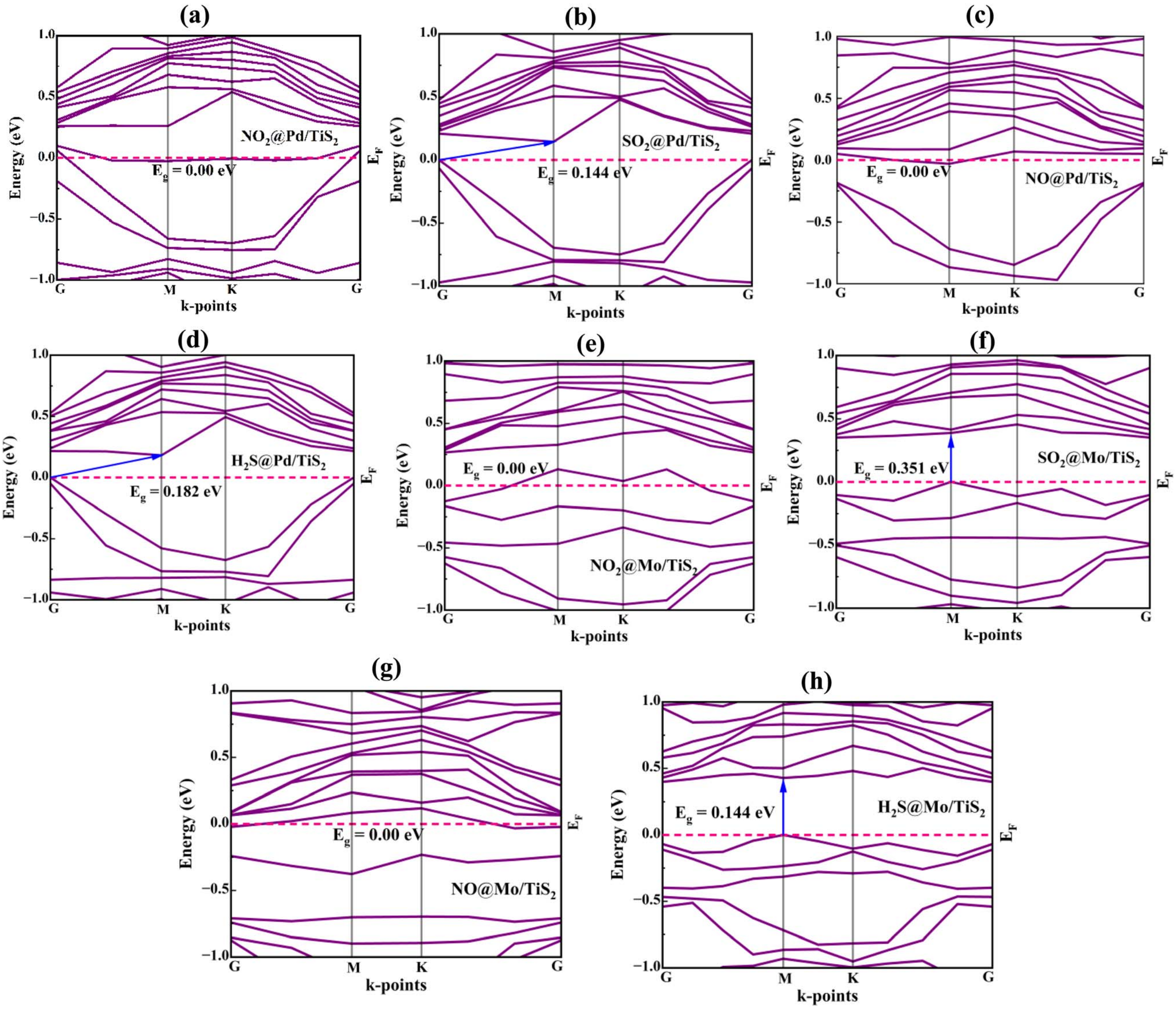

Fig. 7 Electronic band structures (a) NO_2@Pd/TiS_2, (b) SO_2@Pd/TiS_2, (c) NO@Pd/TiS_2, and (d) H_2S@Pd/TiS_2, (e) NO_2@Mo/TiS_2, (f) SO_2@Mo/TiS_2, (g) NO@Mo/TiS_2, and (h) H_2S@Mo/TiS_2.

overlap. These modifications suggest chemisorption, which enhances the sensing response toward SO_2. For NO adsorption, notable changes are observed in the electronic states near the Fermi level. The hybridization of N-2p with Pd-4d orbitals suggests stable chemisorption. Interestingly, H_2S adsorption on Pd/TiS_2 causes relatively weaker changes in the DOS distribution around E_F. The contributions from H-1s and S2-3p (S from H_2S) orbitals are small and show limited overlap with Ti-3d states, indicating a weaker electronic coupling compared to other gases. But the adsorption energy of −0.87 eV and charge transfer of 0.16 electrons confirm that H_2S interacts through chemisorption with small orbital hybridization.

Now, for NO_2 adsorption on Mo/TiS_2, the PDOS reveals pronounced hybridization between the O-2p/N-2p states of NO_2 and the Mo-4d orbitals, extending from −3 eV up to the Fermi level. This indicates a strong chemical interaction. In the case of SO_2 adsorption, considerable changes are also observed in the TDOS, although slightly weaker than NO_2. The PDOS shows strong overlap between O-2p states of SO_2 and Mo-4d orbitals. For NO adsorption, the DOS profile exhibits moderate modification around the Fermi level. The PDOS indicates hybridization between N-2p states of NO and Mo-4d orbitals, confirming the chemisorption nature. In contrast, H_2S adsorption induces only minor changes in the TDOS. The PDOS shows limited contributions from H-1s and S2-3p (from H_2S) states overlapping with the Mo-4d orbitals. This implies a weaker interaction compared to other gases, though it can still be chemisorptive in nature, as the adsorption energy and charge transfer are higher.

3.4 Sensitivity, selectivity, and recovery characteristics

The sensitivity (S) values of pristine, Pd/TiS_2, and Mo/TiS_2 toward various gases were computed for three different temperatures (298, 358, and 398 K) using eqn (5) and are summarized in Table 3. Fig. 9 depicts the sensitivity

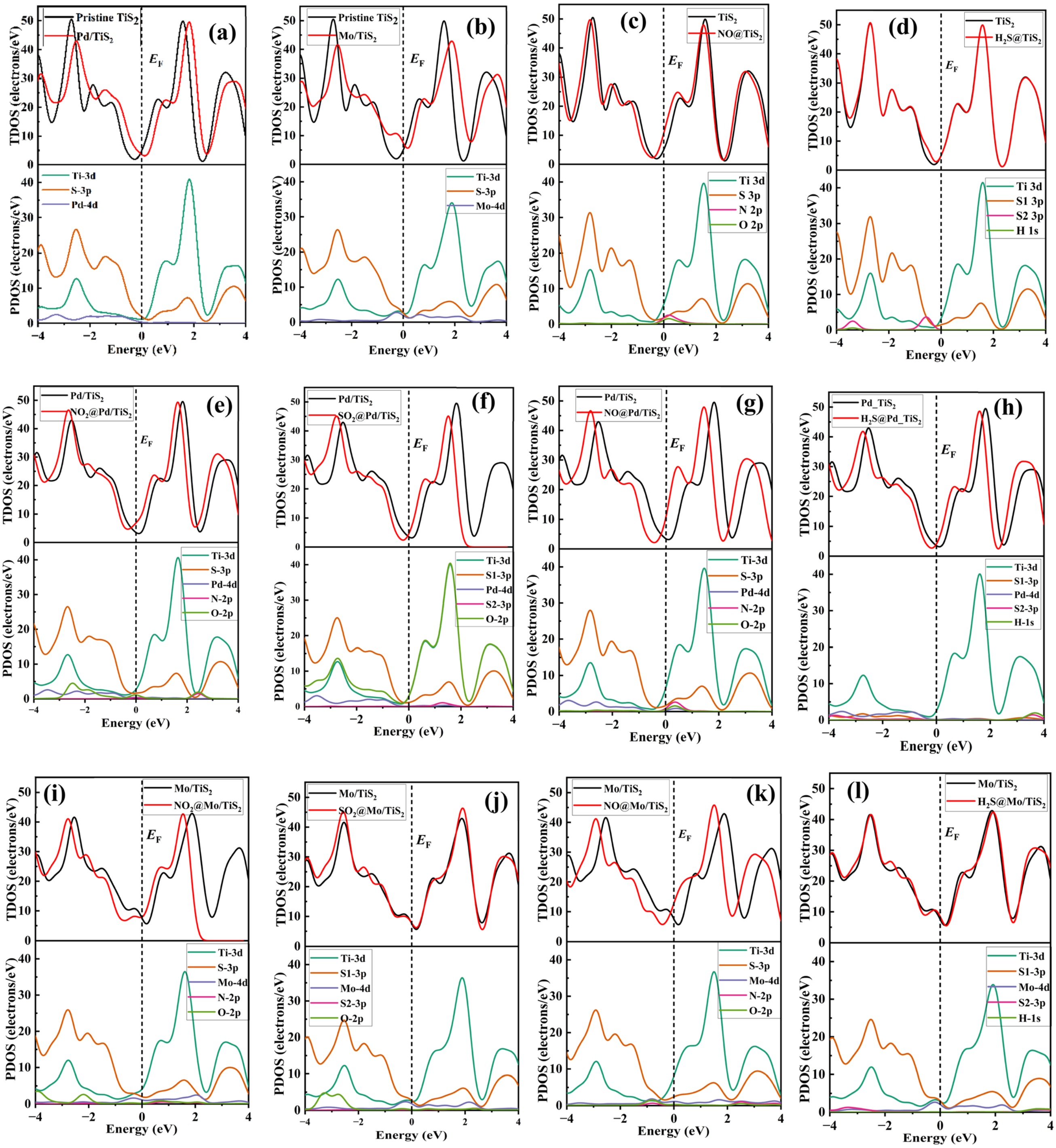

Fig. 8 TDOS and PDOS for various configurations (a) Pd/TiS_2 and (b) Mo/TiS_2, (c) NO@TiS_2, (d) H_2S@TiS_2, (e) NO_2@Pd/TiS_2, (f) SO_2@Pd/TiS_2, (g) NO@Pd/TiS_2, and (h) H_2S@Pd/TiS_2, (i) NO_2@Mo/TiS_2, (j) SO_2@Mo/TiS_2, (k) NO@Mo/TiS_2, and (l) H_2S@Mo/TiS_2.

comparison for adsorbed gas molecules. For all gas molecules, sensitivity decreases with increasing temperature. Pristine TiS_2 shows the highest sensitivity toward NO_2 (5.737), and NO (5.737), both of which are considerably greater than SO_2, and H_2S gases at room temperature. Pd/TiS_2 also exhibits the same pattern of gas sensitivity (NO_2 & NO > H_2S > SO_2), however, the room temperature sensitivity increases for SO_2 (0.719) and H_2S (0.942), and decreases for NO_2 & NO (3.645 for each) compared to pristine TiS_2. Interestingly, Mo/TiS_2 shows significantly the highest sensitivity for NO_2 (392.732) and NO (392.732) at room temperature and at high temperature also holds a significant sensitivity (143.625 at 358 K and 86.727 at 398 K), indicating its strong potential for stable and efficient gas sensor performance across a wide temperature range. In contrast, for SO_2 and H_2S

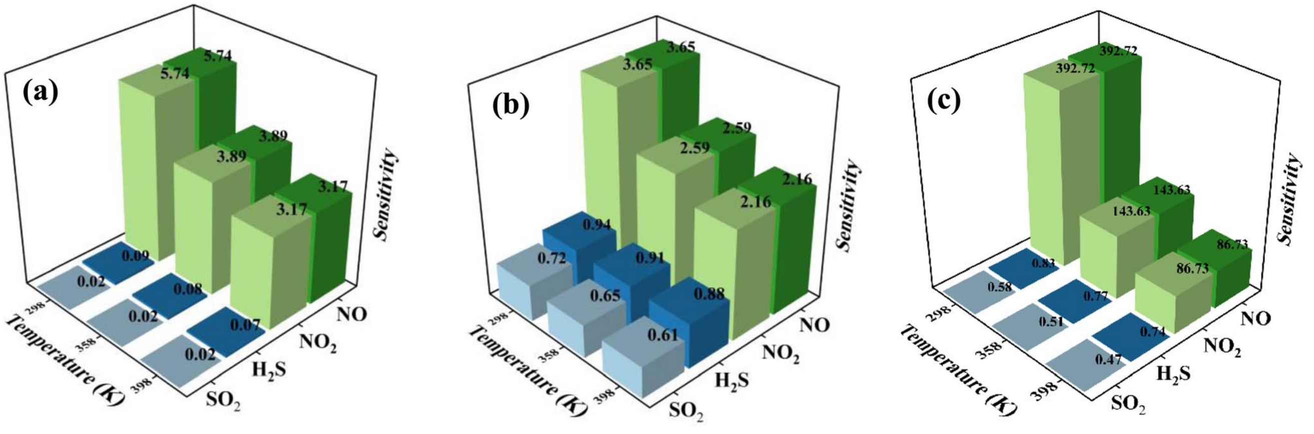

Fig. 9 Sensitivity of gas molecules on adsorption systems, (a) pristine TiS_2, (b) Pd/TiS_2, (c) Mo/TiS_2.

gas molecules, Mo/TiS_2 doesn't show such a huge change in sensitivity. Pd/TiS_2 exhibits better sensitivity for SO_2 and H_2S gases compared to pristine TiS_2 and Mo/TiS_2. However, all three configurations follow the sensitivity order in such that: NO_2 & $NO > H_2S > SO_2$. Overall, despite variations in magnitude among the different monolayer modifications, all three TiS_2-based configurations consistently show the highest sensitivity toward NO_2 and NO, followed by H_2S and then SO_2, highlighting their selective gas-sensing behavior. To further quantify this selectivity, the selectivity coefficients (K) were determined as the ratio of the target gas sensitivity (NO or NO_2) to that of other interfering gases, using eqn (6). The calculated K values at 298 K listed in Table 3 reveal a clear trend in gas discrimination capability across the systems. For pristine TiS_2, NO_2 and NO shows significantly higher selectivity over SO_2 ($K = 301.95$) and H_2S ($K = 61.69$), indicating strong preferential adsorption of NO_2 or NO molecules. Pd functionalization results in a reduction of selectivity, with moderate K values toward SO_2 (5.07) and H_2S (3.87), implying weaker gas discrimination. In contrast, Mo decoration markedly enhances the selectivity, producing exceptionally large K values for SO_2 (681.81) and H_2S (473.16) relative to NO_2 and NO. This trend demonstrates that the Mo/TiS_2 surface possesses superior selectivity toward the target gases, particularly NO_2 and NO, followed by TiS_2, while Pd/TiS_2 exhibits the lowest selectivity. Interestingly, all three systems show similar selectivity towards both NO_2 and NO, that indicates these two gases may not be detected altogether but can be detected if one of them mixed with SO_2, and H_2S based on these selectivity results. This selectivity is calculated from sensitivity comparison only, where sensitivity is calculated from conductivity variation using eqn (5) that depends on band gap change after gas adsorption. After adsorption of NO_2 and NO, all systems band gaps become zero for both gases, that's why the conductivity and sensitivity values remain same for both gases. However, other properties such as, charge transfer, change in work function show different results for NO_2 and NO. These differences may provide alternative measurable signals (work function shifts)[77] for discrimination of NO_2 and NO.

The recovery time (τ) for all adsorbed gases was evaluated using eqn (7) at three different temperatures: 298 K, 348 K, and 398 K, and taking the frequency as 10^{12} Hz, and summarized in Table 4. For pristine TiS_2, all studied gases exhibit ultrafast

Table 4 Recovery time (T_{rec}) at three different temperatures (298 K, 358 K, and 398 K) and work function of gas adsorption systems

Compound	T_{rec} ($T = 298$ K)	T_{rec} ($T = 358$ K)	T_{rec} ($T = 398$ K)	Work function (eV)
TiS_2	—	—	—	5.539
$NO_2@TiS_2$	2.754×10^{-9}	7.302×10^{-10}	3.764×10^{-10}	5.632
$SO_2@TiS_2$	9.333×10^{-9}	2.017×10^{-9}	9.387×10^{-10}	5.561
$NO@TiS_2$	0.0149	0.0003	4.134×10^{-5}	5.255
$H_2S@TiS_2$	1.526×10^{-9}	4.466×10^{-10}	2.419×10^{-10}	5.422
Pd/TiS_2	—	—	—	5.277
$NO_2@Pd/TiS_2$	3.963×10^{12}	2.988×10^{8}	2.616×10^{6}	5.769
$SO_2@Pd/TiS_2$	8.598×10^{-3}	1.86×10^{-4}	2.744×10^{-5}	5.635
$NO@Pd/TiS_2$	0.003	6.586×10^{-5}	1.079×10^{-5}	5.299
$H_2S@Pd/TiS_2$	65.08	0.315	0.022	5.019
Mo/TiS_2	—	—	—	5.316
$NO_2@Mo/TiS_2$	5.544×10^{37}	2.552×10^{29}	1.759×10^{25}	5.465
$SO_2@Mo/TiS_2$	1.21×10^{5}	165.339	6.157	5.81
$NO@Mo/TiS_2$	6.8×10^{45}	1.38×10^{36}	2.003×10^{31}	5.358
$H_2S@Mo/TiS_2$	1.54×10^{10}	2.95×10^{6}	4.11×10^{4}	5.186

recovery times in the range of 10^{-9} to 10^{-5} s. This indicates highly reversible physisorption and may not retain gases long enough for accurate detection. These systems can be used only when a very fast recovery is required. NO_2@Pd/TiS_2 shows exceedingly long recovery times (up to 10^{12} s at 298 K), indicative of strong chemisorption. Although this enhances gas capture, the excessively slow desorption hinders sensor reusability and response speed. In contrast, SO_2@Pd/TiS_2 displays moderate recovery times (from 8.598×10^{-3} s at 298 K to 2.744×10^{-5} s at 398 K), suggesting a balanced adsorption–desorption behavior favorable for sensing. The recovery time for H_2S@Pd/TiS_2 is 65.08 s at 298 K and decreases to 0.022 s at 398 K, which indicates that H_2S can be detected by Pd/TiS_2 at room temperature and also slightly elevated temperatures. Mo decoration results in even stronger gas adsorption, as evidenced by extremely high recovery times for NO_2 and NO (10^{25} to 10^{45} s), rendering them impractical under ambient conditions due to irreversible binding. However, SO_2 and H_2S on Mo/TiS_2 show more manageable recovery behaviors at elevated temperatures (*e.g.*, 6.157 s for SO_2 at 398 K and 4.11×10^4 s for H_2S at 398 K), suggesting these systems could be viable for high-temperature sensing applications.

3.5 Work function analysis

To further evaluate the gas sensing performance of pristine TiS_2, Pd/TiS_2, and Mo/TiS_2 upon the adsorption of NO_2, SO_2, NO, and H_2S, the corresponding WF values were calculated using eqn (8). Fig. 10 presents the WF variations, and the detailed results are summarized in Table 4. The work function (WF) of pristine TiS_2 was calculated as 5.539 eV, which provides the baseline for comparison with gas-adsorbed and decorated systems. Upon adsorption of gases on pristine TiS_2, slight variations in WF were observed: NO_2 (5.632 eV) and SO_2 (5.561 eV) increased the WF, indicating weak electron withdrawal from the surface, while NO (5.255 eV) and H_2S (5.422 eV) reduced the WF, suggesting electron donation to the substrate. These modest changes imply limited charge transfer between pristine TiS_2 and the target gases.

Decorating with Pd significantly modified the surface electronic structure, lowering the WF to 5.277 eV, thereby facilitating electron mobility. When gases were adsorbed on Pd/TiS_2, pronounced WF variations were observed: NO_2 (5.769 eV) and SO_2 (5.635 eV) induced substantial increases, reflecting strong electron transfer from the substrate to the oxidizing gases. In contrast, H_2S adsorption reduced the WF to 5.019 eV, highlighting enhanced electron donation and strong interaction with the Pd-modified surface.

Similarly, Mo decoration reduced the WF to 5.316 eV, improving the electron transfer capability of TiS_2. Among the gases, SO_2 adsorption produced the highest WF (5.81 eV), indicating strong interaction and significant charge redistribution at the Mo/TiS_2 surface. NO_2 and NO also caused moderate increases to 5.465 eV and 5.358 eV, respectively, while H_2S lowered the WF to 5.186 eV, suggesting its electron-donating behavior.

Overall, these results demonstrate that Pd and Mo decoration effectively lowers the WF, improves electron mobility, and enhances the gas sensing performance of TiS_2. Interestingly, the trend in work function variation does not perfectly coincide with the net charge transfer values obtained from Hirshfeld charge analysis listed in Table 2. SO_2 adsorption on Mo/TiS_2 yields a relatively small charge transfer than other gases but induces one of the largest work function shifts. This discrepancy arises because the work function is governed not only by charge magnitude but also by the adsorption-induced surface dipole, which depends on charge redistribution, molecular orientation, and interface effects.[78,79] Moreover, Hirshfeld analysis provides only an approximate measure of charge transfer, often underestimating interfacial polarization, while the work function reflects the overall electrostatic response, including dipole formation and Pauli push-back effects.[80,81] However, Pd and Mo decoration improve the gas sensing performance of TiS_2 based on both work function analysis and Hersfield charge transfer analysis.

3.6 Comparative analysis of gas-sensing performance with reported studies

Table 5 compares the gas-sensing properties of Pd/TiS_2 and Mo/TiS_2 systems investigated in this work with previously reported materials toward NO_2, SO_2, NO, and H_2S gases. The parameters considered include adsorption energy (E_{ads}), charge transfer (ΔQ), and sensitivity (S) at 298 K.

For NO_2 sensing, the Mo/TiS_2 system exhibits the highest adsorption energy (−2.942 eV) among all the compared

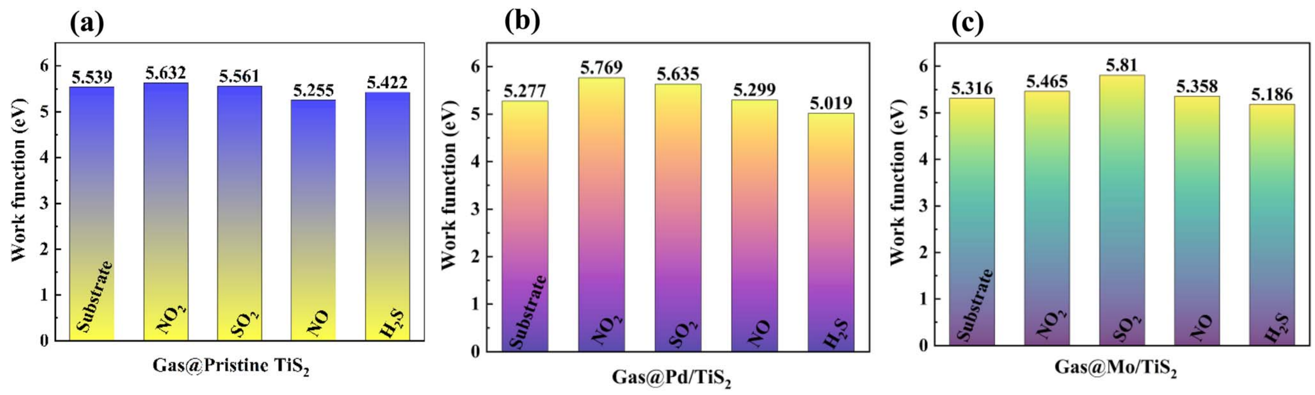

Fig. 10 Work function comparison for (a) pristine TiS_2, (b) Pd/TiS_2, (c) Mo/TiS_2 to different gases.

Table 5 Comparison of gas sensing properties of NO_2, SO_2, NO, and H_2S gases with other studies

System	Gas	Adsorption energy, E_{ads} (eV)	Charge transfer, ΔQ (e)	Sensitivity, S ($T = 298$ K)	References
Li/TiS_2	NO_2	−0.73	−0.253	—	82
Pt/ZrS_2	NO_2	−0.685	−0.130	0.99	72
Pd/TiS_2	NO_2	−0.979	−0.21	3.645	This work
Mo/TiS_2	NO_2	−2.942	−0.22	392.723	This work
Li/TiS_2	SO_2	−0.95	0.014	—	82
Pd/ZrS_2	SO_2	−1.02	−0.08	—	83
Rh/HfS_2	SO_2	−0.406	−0.083	—	85
Pd/TiS_2	SO_2	−0.588	−0.09	0.719	This work
Mo/TiS_2	SO_2	−1.01	−0.1	0.576	This work
Li/TiS_2	NO	−0.99	0.186	—	82
Pt/ZrS_2	NO	−0.944	0.0511	5.74	72
Pd/TiS_2	NO	−1.455	0.07	3.645	This work
Mo/TiS_2	NO	−3.421	−0.17	392.723	This work
Rh/$ZrSe_2$	H_2S	−1.274	0.250	—	84
Pt/ZrS_2	H_2S	−0.905	0.228	11.08	72
Pd/TiS_2	H_2S	−0.817	0.16	0.906	This work
Mo/TiS_2	H_2S	−1.312	0.17	0.772	This work

materials. In contrast, Pd/TiS_2 shows relatively moderate E_{ads} of −0.979 eV, which still surpasses that of Li/TiS_2 (−0.73 eV)[82] and Pt/ZrS_2 (−0.685 eV).[72] The charge transfer values also support this trend, where both Pd/TiS_2 ($-0.21e$) and Mo/TiS_2 ($-0.22e$) exhibit greater electron exchange compared to other reported systems. The exceptionally high sensitivity value for Mo/TiS_2 (392.723) further confirms its superior response capability toward NO_2 gas. In the case of SO_2 adsorption, both Pd/TiS_2 and Mo/TiS_2 display favorable adsorption characteristics with E_{ads} values of −0.588 eV and −1.01 eV, respectively. These are comparable to Pd/ZrS_2 (−1.02 eV)[83] and Li/TiS_2 (−0.95 eV),[82] suggesting effective interaction while maintaining good reversibility. The charge transfer for Mo/TiS_2 ($-0.1e$) is slightly higher than that of Pd/TiS_2 ($-0.09e$), both are higher compared to other reported values. For NO gas, Mo/TiS_2 again demonstrates remarkably higher adsorption energy (−3.421 eV) compared to Pd/TiS_2 (−1.455 eV) and other materials such as Li/TiS_2 (−0.99 eV)[82] and Pt/ZrS_2 (−0.944 eV).[72] Mo/TiS_2 also show extraordinarily high sensitivity (392.723) compared to other materials, indicating its excellent potential for NO detection. Regarding H_2S sensing, Pd/TiS_2 and Mo/TiS_2 exhibit adsorption energies of −0.817 eV and −1.312 eV, respectively, which are comparable to or higher than those of previously reported systems such as Pt/ZrS_2 (−0.905 eV)[72] and Rh/$ZrSe_2$ (−1.274 eV).[84] Both systems also show notable charge transfer values ($0.16e$ for Pd/TiS_2 and $0.17e$ for Mo/TiS_2) comparable to other materials. However, Pd/TiS_2 and Mo/TiS_2 show poorer sensitivity compared to Pt/ZrS_2.

4. Conclusions

This first-principles density functional theory study comprehensively investigated the gas-sensing properties of pristine and transition metal Pd/Mo-decorated TiS_2 monolayers toward industrial toxic gases (NO_2, SO_2, NO, H_2S). The thermodynamic stability of pristine TiS_2 was confirmed through negative cohesive energy, and the hollow site was identified as the most energetically favorable position for both Pd and Mo decoration, where strong covalent bonds were formed between Pd/Mo–S atoms. Pristine TiS_2 exhibited strong chemisorption only for NO, while displaying weak physisorption for NO_2, SO_2, and H_2S. However, both Pd and Mo decoration significantly enhanced the adsorption characteristics for all target gases, transforming weak physisorption into strong chemisorption. Mo/TiS_2, in particular, demonstrated the strongest adsorption energies for all target gases. Electronically, adsorption of NO_2 and NO on both decorated systems (especially Mo/TiS_2) consistently led to a metallic state (0 eV band gap), indicating a drastic increase in electrical conductivity and high sensitivity. This enhancement was corroborated by density of states analysis, which revealed significant orbital hybridization and efficient charge transfer between gas molecules and the decorated metal atoms. In terms of sensing performance, Mo/TiS_2 showed exceptionally high sensitivity to NO_2 and NO (392.732 at room temperature). While pristine TiS_2 offered ultrafast recovery due to physisorption, Mo/TiS_2 exhibited excessively long recovery times for NO_2 and NO at ambient conditions, suggesting irreversible binding. However, SO_2 and H_2S on Mo/TiS_2 demonstrated more manageable recovery (6.571 and 4.11×10^4 s) at elevated temperatures, making them viable for high-temperature applications. Pd/TiS_2 provided a balanced adsorption–desorption for SO_2, NO, and H_2S at room temperature. Work function analysis further supported that Pd and Mo decoration effectively lowered the work function of TiS_2, enhancing electron mobility and overall gas sensing performance. These findings suggest that transition metal decoration, particularly with Mo and Pd, is an effective strategy to greatly enhance the gas-sensing performance of TiS_2 monolayers. Though Mo/TiS_2 exhibits high sensitivity and strong adsorption toward NO_2 and NO, its slow desorption behavior limits practical application, whereas Pd/TiS_2 shows comparatively more favorable recovery characteristics. These insights offer useful guidance for the rational design of next-generation 2D material-based gas sensors.

Author contributions

Tasmi Akter: conceptualization, writing – original draft, methodology, software, validation, formal analysis, investigation, data curation, visualization. Md. Jahirul Islam: conceptualization, writing – review & editing, validation, supervision. Md. Tawabur Rahman: writing – review & editing, validation, supervision. Jahirul Islam: writing – review & editing, visualization, validation.

Conflicts of interest

The authors declare that there are no known financial or personal conflicts of interest that could have influenced the work presented in this paper.

Data availability

The data supporting the findings of this study are available from the corresponding authors upon reasonable request.

Supplementary information is available. See DOI: https://doi.org/10.1039/d5ra06850a.

Acknowledgements

The computational work of this research was performed at the Computational Materials Science Laboratory in the Department of Materials Science and Engineering at Khulna University of Engineering & Technology, Khulna 9203, Bangladesh.

References

1 K. A. Abdur Nur, M. S. Hasan Khan and M. R. Islam, Superior selectivity for NH_3 (NO_2) gas molecules in In_2 SSe (Ga_2 SSe) Janus materials: a first-principles study, *Phys. Scr.*, 2024, **99**(9), 095934, DOI: 10.1088/1402-4896/ad69d2.

2 L. Lin, *et al.*, Effects of V and Mo dopants on electronic structures, magnetic and optical properties of ZrSe2: First-principles calculations, *Phys. B*, 2023, **655**, 414733, DOI: 10.1016/j.physb.2023.414733.

3 H. Cui, M. Ran, X. Peng and G. Zhang, First-principles design of noble metal (Rh and Pd) dispersed Janus WSTe monolayer for toxic gas sensing applications, *J. Environ. Chem. Eng.*, 2024, **12**(2), 112047, DOI: 10.1016/j.jece.2024.112047.

4 D. B. Patil, *et al.*, Facile synthesis of MoO3 nanoplates based NO2 gas sensor: Ultra-selective and sensitive, *Chem. Phys. Lett.*, 2021, **782**, 139025, DOI: 10.1016/j.cplett.2021.139025.

5 T. V. Vu and K. D. Pham, The theoretical prediction of the structural characteristics and SO_2 adsorption-sensing properties of pristine HfS_2 and TM-doped HfS_2 monolayers (TM = Ni, Pd, or Pt), *New J. Chem.*, 2023, **47**(37), 17252–17260, DOI: 10.1039/d3nj01053h.

6 R. Zhang, D. Fu, J. Ni, C. Sun and S. Song, Adsorption for SO2 gas molecules on B, N, P and Al doped MoS2: The DFT study, *Chem. Phys. Lett.*, 2019, **715**, 273–277, DOI: 10.1016/j.cplett.2018.11.054.

7 C.-Y. Lin, *et al.*, Using a TiO2/ZnO double-layer film for improving the sensing performance of ZnO based NO gas sensor, *Sens. Actuators, B*, 2011, **157**(2), 361–367, DOI: 10.1016/j.snb.2011.04.056.

8 T. Akamatsu, T. Itoh, N. Izu and W. Shin, NO and NO2 Sensing Properties of WO3 and Co3O4 Based Gas Sensors, *Sensors*, 2013, **13**(9), 12467–12481, DOI: 10.3390/s130912467.

9 L. Wan, D. Chen, W. Zeng, J. Li and S. Xiao, Hazardous gas adsorption of Janus HfSeTe monolayer adjusted by surface vacancy defect: A DFT study, *Surf. Interfaces*, 2022, **34**, 102316, DOI: 10.1016/j.surfin.2022.102316.

10 G. Soydan, A. F. Ergenc, A. T. Alpas and N. Solak, Development of an NO2 Gas Sensor Based on Laser-Induced Graphene Operating at Room Temperature, *Sensors*, 2024, **24**(10), 3217, DOI: 10.3390/s24103217.

11 L. Yang, *et al.*, Highly sensitive, room-temperature hydrogen sulfide gas sensor based on tungsten trioxide/laser-induced graphene, *Chem. Eng. J.*, 2025, **521**, 166393, DOI: 10.1016/j.cej.2025.166393.

12 D. Talukdar, D. Mohanta and G. A. Ahmed, Nitrogen doped compound defect in black phosphorene for enhanced gas sensing, *Surf. Interfaces*, 2024, **51**, 104699, DOI: 10.1016/j.surfin.2024.104699.

13 A. Allosh, *et al.*, Tuning phosphorene and MoS 2 2D materials for detecting volatile organic compounds associated with respiratory diseases, *RSC Adv.*, 2024, **14**(3), 1803–1812, DOI: 10.1039/D3RA07685G.

14 H. Zuo, S. Zhan, W. Xu, X. Wei and J. Cao, Theoretical approaches toward designing sensitive materials for carbon nanotube-based field-effect transistor gas sensors, *Sens. Actuators, B*, 2024, **409**, 135604, DOI: 10.1016/j.snb.2024.135604.

15 S. M. Aalam, M. Sarvar, M. Sadiq and J. Ali, A Highly Sensitive Surface-Modified Porous Carbon Nanotube-Based Sensor for Ammonia Gas Detection, *ACS Omega*, 2024, **9**(4), 4486–4496, DOI: 10.1021/acsomega.3c07244.

16 A. Mirzaei, J.-Y. Kim, H. W. Kim and S. S. Kim, Resistive Gas Sensors Based on 2D TMDs and MXenes, *Acc. Chem. Res.*, 2024, **57**(16), 2395–2413, DOI: 10.1021/acs.accounts.4c00323.

17 M. Hjiri, *et al.*, Ammonia gas sensors based on undoped and Ca-doped ZnO nanoparticles, *RSC Adv.*, 2024, **14**(8), 5001–5011, DOI: 10.1039/D3RA08181H.

18 V. K. Premkumar, *et al.*, Influence of ZnO hexagonal pyramid nanostructures for highly sensitive and selective NO2 gas sensor, *J. Alloys Compd.*, 2024, **994**, 174625, DOI: 10.1016/j.jallcom.2024.174625.

19 S. Li, *et al.*, Controllable synthesis of heterostructured CuO–ZnO microspheres for NO2 gas sensors, *Sens. Actuators, B*, 2024, **417**, 136179, DOI: 10.1016/j.snb.2024.136179.

20 Y. Duan, X. Yang, Z. Qin, Y. Tian, Y. Wang and J. Wang, Exploration of the Transition Metal-Doped CrS2 Monolayer as a Gas Sensor of Toxic Gases Based on the Density Functional Theory Method, *Langmuir*, 2025, **41**(23), 15068–15083, DOI: 10.1021/acs.langmuir.5c01333.

21 K. Wongphen, P. Ruttanapunt, S. Khammuang, T. Hussain and K. Kotmool, Modulating WS2 surface reactivity *via* Nb

decoration: A DFT study of gas interaction, sensing, and storage potential, *Appl. Surf. Sci.*, 2025, 164507, DOI: 10.1016/j.apsusc.2025.164507.

22 H. Wang, *et al.*, Gas sensing materials roadmap, *J. Phys.:Condens. Matter*, 2021, **33**(30), 303001, DOI: 10.1088/1361-648x/abf477.

23 M. A. H. Khan, M. V. Rao and Q. Li, Recent Advances in Electrochemical Sensors for Detecting Toxic Gases: NO2, SO2 and H2S, *Sensors*, 2019, **19**(4), 905, DOI: 10.3390/s19040905.

24 A. Kushwaha, N. R. Bharti, A. Sharma, S. K. Kedia, G. Gupta and N. Goel, Enhanced NO2 Gas Sensing in Nanocrystalline MoS2 via Swift Heavy Ion Irradiation: An Experimental and DFT Study, *ACS Sens.*, 2024, **9**(11), 5966–5975, DOI: 10.1021/acssensors.4c01812.

25 R. Hajlaoui, S. Baachaoui, S. Ben Aoun, S. Ridene and N. Raouafi, Surface Tailoring of MoS2 Nanosheets with Substituted Aromatic Diazonium Salts for Gas Sensing: A DFT Study, *ACS Omega*, 2024, **9**(36), 37953–37964, DOI: 10.1021/acsomega.4c04506.

26 F. M. A. Altalbawy, *et al.*, Pd and Pt transition metal decorated WS2 nanosheets as efficient gas sensors for SOx molecules: A comparative DFT study, *Mater. Chem. Phys.*, 2026, **347**, 131385, DOI: 10.1016/j.matchemphys.2025.131385.

27 S. Kamila, M. Kandasamy, B. Chakraborty and B. K. Jena, Recent development on engineered TMDs for charge storage performance: Experimental and theoretical investigations, *J. Energy Storage*, 2024, **89**, 111614, DOI: 10.1016/j.est.2024.111614.

28 S. Li, P. Das, X. Wang, C. Li, Z.-S. Wu and H.-M. Cheng, Insights on Fabrication Strategies and Energy Storage Mechanisms of Transition Metal Dichalcogenides Cathodes for Aqueous Zn-Based Batteries, *Small*, 2025, 2410036, DOI: 10.1002/smll.202410036.

29 M. Kumari, N. K. Singh, V. Kantipudi and M. Sahoo, Design and investigation of charge plasma-based TMD heterojunction TFET biosensor for ultrasensitive detection, *Sci. Rep.*, 2025, **15**(1), 15195, DOI: 10.1038/s41598-024-84677-6.

30 X. Wang, M. Xiang, B. Abulimiti, J. Ma and W. Hu, Rational Design of Zero-Dimensional Gold Cluster/Two-Dimensional TMD Heterostructures for Enhanced Photocatalytic and Optoelectronic Performance, *Nano Lett.*, 2025, **25**(24), 9801–9808, DOI: 10.1021/acs.nanolett.5c02192.

31 S. Zhao, *et al.*, Tunable WSe2–MoSe2 Lateral Heterojunction Photodetector Based on Piezoelectric and Flexoelectric Effects, *ACS Appl. Mater. Interfaces*, 2024, **16**(49), 67889–67899, DOI: 10.1021/acsami.4c09423.

32 T. S. Wagh, S. H. Mane, S. B. Bansode and M. K. Deore, Hydrothermal synthesis of nanostructured titanium disulfide (TiS2) for detection of NO2 gas and its characterization study, *J. Mater. Sci.:Mater. Electron.*, 2024, **35**(19), 1341, DOI: 10.1007/s10854-024-12991-w.

33 O. Asif, F. Azadian and A. C. Rastogi, Titanium Disulphide (TiS2) Dichalcogenide Thin Films as Inorganic Hole Transport Layer for Perovskite Solar Cells Synthesized from Ionic Liquid Electrodeposition, *MRS Adv.*, 2020, **5**(64), 3555–3564, DOI: 10.1557/adv.2020.412.

34 M. Talib, *et al.*, Development of ultra-sensitive broadband photodetector: a detailed study on hidden photodetection-properties of TiS2 nanosheets, *J. Mater. Res. Technol.*, 2021, **14**, 1243–1254, DOI: 10.1016/j.jmrt.2021.07.032.

35 K. H. Park, J. Choi, H. J. Kim, D. Oh, J. R. Ahn and S. U. Son, Unstable Single-Layered Colloidal TiS_2 Nanodisks, *Small*, 2008, **4**(7), 945–950, DOI: 10.1002/smll.200700804.

36 M. Barawi, *et al.*, Hydrogen Storage by Titanium Based Sulfides: Nanoribbons (TiS3) and Nanoplates (TiS2), *J. Electr. Eng.*, 2015, **3**(1), 23–29, DOI: 10.17265/2328-2223/2015.01.004.

37 T. S. Wagh, S. H. Mane, S. B. Bansode and M. K. Deore, Hydrothermal synthesis of nanostructured titanium disulfide (TiS2) for detection of NO2 gas and its characterization study, *J. Mater. Sci.:Mater. Electron.*, 2024, **35**(19), 1341, DOI: 10.1007/s10854-024-12991-w.

38 N. Sakhuja, R. K. Jha, R. Chaurasiya, A. Dixit and N. Bhat, 1T-Phase Titanium Disulfide Nanosheets for Sensing H2S and O2, *ACS Appl. Nano Mater.*, 2020, **3**(4), 3382–3394, DOI: 10.1021/acsanm.0c00127.

39 S. Manzoor, M. Talib, S. M. Novikov, A. V. Arsenin, V. S. Volkov and P. Mishra, Physisorption-Mediated Charge Transfer in TiS2 Nanodiscs: A Room Temperature Sensor for Highly Sensitive and Reversible Carbon Dioxide Detection, *ACS Sens.*, 2023, **8**(9), 3435–3447, DOI: 10.1021/acssensors.3c00931.

40 S. Sharma, S. Singh, R. C. Singh and S. Sharma, Structural transformation and room temperature ammonia sensing properties of TiS2 nanostructures, *SN Appl. Sci.*, 2020, **2**(5), 887, DOI: 10.1007/s42452-020-2647-x.

41 J. Wang, *et al.*, Tailoring the sensing capability of 2H-MoSe2 via 3*d* transition metal decoration, *Appl. Surf. Sci.*, 2023, **610**, 155399, DOI: 10.1016/j.apsusc.2022.155399.

42 H. Wu, W. Zhang, H. Yuan, G. Lin, H. Xie and T. Jiang, Enhanced H2 sensing performance of Pd decorated MoS2: Experimental and DFT Insights, *J. Alloys Compd.*, 2025, **1010**, 178139, DOI: 10.1016/j.jallcom.2024.178139.

43 N. H. Ali and L. F. Al-Badry, Mo-PtTe2 monolayer as a promising biosensor for prediagnosis of lung cancer: A DFT study, *Comput. Theor. Chem.*, 2023, **1230**, 114379, DOI: 10.1016/j.comptc.2023.114379.

44 M.-Q. Zhu, X.-F. Wang and P. Vasilopoulos, Transition metal-doped ZrS_2 monolayer as potential gas sensor for CO_2, SO_2, and NO_2: density functional theory and non-equilibrium Green's functions' analysis, *J. Phys. D:Appl. Phys.*, 2025, **58**(13), 135306, DOI: 10.1088/1361-6463/adafb7.

45 T. V. Vu and K. D. Pham, The theoretical prediction of the structural characteristics and SO_2 adsorption-sensing properties of pristine HfS_2 and TM-doped HfS_2 monolayers (TM = Ni, Pd, or Pt), *New J. Chem.*, 2023, **47**(37), 17252–17260, DOI: 10.1039/d3nj01053h.

46 M. Dong, *et al.*, A Study Based on the First-Principle Study of the Adsorption and Sensing Properties of Mo-Doped WSe2 for N2O, CO2, and CH4, *Chemosensors*, 2024, **12**(9), 192, DOI: 10.3390/chemosensors12090192.

47 L. Huang, T. Li, W. Zeng and Q. Zhou, Two-dimensional Mo3-TiS2 monolayer hosting high moisture resistance and abundant surface-chemisorbed oxygen for effective detection of SF6 decomposition gases: Atomic-scale study, *Appl. Surf. Sci.*, 2024, **670**, 160651, DOI: **10.1016/j.apsusc.2024.160651**.

48 Z. Saleem, S. S. Alarfaji, H. Shaheen, A. Majid and M. I. Khan, DFT investigation of pristine and li-functionalized TiS2 monolayers for toxic gas sensing applications, *J. Environ. Chem. Eng.*, 2025, **13**(5), 118534, DOI: **10.1016/j.jece.2025.118534**.

49 T. Akter and J. Islam, DFT Study on the Sensing of Industrial Toxic Gases (XO2, X = N, S) by TiS2 TMD Monolayer, *presented at the 2025 International Conference on Quantum Photonics, Artificial Intelligence, and Networking (QPAIN)*, IEEE, Rangpur, Bangladesh, 2025.

50 P. J. D. Lindan, *et al.*, First-principles simulation: ideas, illustrations and the CASTEP code, *J. Phys.:Condens. Matter*, 2002, **14**(11), 2717–2744, DOI: **10.1088/0953-8984/14/11/301**.

51 W. Kohn and L. J. Sham, Self-Consistent Equations Including Exchange and Correlation Effects, *Phys. Rev.*, 1965, **140**(4A), A1133–A1138, DOI: **10.1103/PhysRev.140.A1133**.

52 J. P. Perdew, *et al.*, Erratum: Atoms, molecules, solids, and surfaces: Applications of the generalized gradient approximation for exchange and correlation, *Phys. Rev. B:Condens. Matter Mater. Phys.*, 1993, **48**(7), 4978, DOI: **10.1103/PhysRevB.48.4978.2**.

53 A. Tkatchenko and M. Scheffler, Accurate Molecular Van Der Waals Interactions from Ground-State Electron Density and Free-Atom Reference Data, *Phys. Rev. Lett.*, 2009, **102**(7), 073005, DOI: **10.1103/PhysRevLett.102.073005**.

54 D. Vanderbilt, Soft self-consistent pseudopotentials in a generalized eigenvalue formalism, *Phys. Rev. B:Condens. Matter Mater. Phys.*, 1990, **41**(11), 7892–7895, DOI: **10.1103/PhysRevB.41.7892**.

55 J. D. Head and M. C. Zerner, A Broyden—Fletcher—Goldfarb—Shanno optimization procedure for molecular geometries, *Chem. Phys. Lett.*, 1985, **122**(3), 264–270, DOI: **10.1016/0009-2614(85)80574-1**.

56 L. Lin, *et al.*, Effects of V and Mo dopants on electronic structures, magnetic and optical properties of ZrSe2: First-principles calculations, *Phys. B*, 2023, **655**, 414733, DOI: **10.1016/j.physb.2023.414733**.

57 K. Hossain, M. T. Ahmed, R. A. Rabu and F. Ahmed, First-principles investigations of As-doped tetragonal boron nitride nanosheets for toxic gas sensing applications, *Nanoscale Adv.*, 2025, **7**(1), 354–369, DOI: **10.1039/D4NA00739E**.

58 G. P. Srivastava and D. Weaire, The theory of the cohesive energies of solids, *Adv. Phys.*, 1987, **36**(4), 463–517, DOI: **10.1080/00018738700101042**.

59 S. U. D. Shamim, *et al.*, Understanding Na-ion adsorption in nitrogen doped graphene oxide anode for rechargeable sodium ion batteries, *Appl. Surf. Sci.*, 2022, **579**, 152147, DOI: **10.1016/j.apsusc.2021.152147**.

60 M.-Q. Zhu, X.-F. Wang and P. Vasilopoulos, Transition metal-doped ZrS_2 monolayer as potential gas sensor for CO_2 , SO_2 , and NO_2 : density functional theory and non-equilibrium Green's functions' analysis, *J. Phys. D:Appl. Phys.*, 2025, **58**(13), 135306, DOI: **10.1088/1361-6463/adafb7**.

61 R. Carbó-Dorca and P. Bultinck, Quantum Mechanical Basis for Mulliken Population Analysis, *J. Math. Chem.*, 2004, **36**(3), 231–239, DOI: **10.1023/B:JOMC.0000044221.23647.20**.

62 X. Li, G. Zhao, K. Xie, P. Wang, C. Zhang and L. Lin, Cu-decorated HfS2 and Cu-embedded HfS2 for adsorption and gas sensing of lithium-ion thermal runaway gases: A DFT study, *Surf. Interfaces*, 2024, **46**, 104028, DOI: **10.1016/j.surfin.2024.104028**.

63 G. Guo, J. Min, Y. Xu, Y. Zhou and G. Xu, Gas Sensing Properties of Pd-Decorated GeSe Monolayer toward Formaldehyde and Benzene Molecules: A First-Principles Study, *Langmuir*, 2024, **40**(1), 997–1006, DOI: **10.1021/acs.langmuir.3c03221**.

64 G. Fan, X. Wang, X. Tu, H. Xu, Q. Wang and X. Chu, Density functional theory study of Cu-doped BNNT as highly sensitive and selective gas sensor for carbon monoxide, *Nanotechnology*, 2021, **32**(7), 075502, DOI: **10.1088/1361-6528/abc57a**.

65 T. Jiang, W. Zhang, T. Zhang, H. Yuan, M. Bi and X. Zhou, Adsorption and gas-sensing performances of C2H2, C2H4, CO, H2 in transformer oil on Pt-doped MoTe2 monolayer: A DFT study, *Phys. E*, 2023, **146**, 115568, DOI: **10.1016/j.physe.2022.115568**.

66 K. Hossain, M. T. Ahmed, R. A. Rabu and F. Ahmed, First-principles investigations of As-doped tetragonal boron nitride nanosheets for toxic gas sensing applications, *Nanoscale Adv.*, 2025, **7**(1), 354–369, DOI: **10.1039/d4na00739e**.

67 S. Arrhenius, Über die Dissociationswärme und den Einfluss der Temperatur auf den Dissociationsgrad der Elektrolyte, *Z. Phys. Chem.*, 1889, **4**(1), 96–116.

68 H. Cui and P. Jia, Doping effect of small Rhn (n = 1–4) clusters on the geometric and electronic behaviors of MoS2 monolayer: A first-principles study, *Appl. Surf. Sci.*, 2020, **526**, 146659, DOI: **10.1016/j.apsusc.2020.146659**.

69 D. Chen, *et al.*, A First-Principles Study of the SF6 Decomposed Products Adsorbed Over Defective WS2 Monolayer as Promising Gas Sensing Device, *IEEE Trans. Device Mater. Reliab.*, 2019, **19**(3), 473–483, DOI: **10.1109/TDMR.2019.2919773**.

70 X. Peng, D. Liu, F. Zhao and C. Tang, Gas sensing properties of Mg-doped graphene for H_2S, SO_2, SOF_2, and SO_2F_2 based on DFT, *Int. J. Quantum Chem.*, 2022, **122**(22), e26989, DOI: **10.1002/qua.26989**.

71 G. Kresse and J. Furthmüller, Efficiency of ab-initio total energy calculations for metals and semiconductors using a plane-wave basis set, *Comput. Mater. Sci.*, 1996, **6**(1), 15–50, DOI: **10.1016/0927-0256(96)00008-0**.

72 X.-Q. Lin, X. Zhang, Y.-Y. Qin and Y.-G. Yao, Tuning the Gas Sensing Properties of ZrS2 Monolayers via Pt Modification: Insights from DFT Simulations, *Langmuir*, 2025, **41**(10), 6801–6815, DOI: **10.1021/acs.langmuir.4c05040**.

73 H. Kasai, *et al.*, X-ray electron density investigation of chemical bonding in van der Waals materials, *Nat. Mater.*, 2018, **17**(3), 249–252, DOI: 10.1038/s41563-017-0012-2.

74 A. A. Haidry, *et al.*, Unveiling the optoelectronic properties of bulk, monolayer, and bilayer TiS2: A DFT approach, *Mater. Today Commun.*, 2024, **41**, 110601, DOI: 10.1016/j.mtcomm.2024.110601.

75 B. Cordero, *et al.*, Covalent radii revisited, *Dalton Trans.*, 2008, (21), 2832, DOI: 10.1039/b801115j.

76 R. Gao, Y. Yong, X. Yuan, S. Hu, Q. Hou and Y. Kuang, First-Principles Investigation of Adsorption Behaviors and Electronic, Optical, and Gas-Sensing Properties of Pure and Pd-Decorated GeS_2 Monolayers, *ACS Omega*, 2022, **7**(50), 46440–46451, DOI: 10.1021/acsomega.2c05142.

77 A. Oprea, N. Bârsan and U. Weimar, Work function changes in gas sensitive materials: Fundamentals and applications, *Sens. Actuators, B*, 2009, **142**(2), 470–493, DOI: 10.1016/j.snb.2009.06.043.

78 T. C. Leung, C. L. Kao, W. S. Su, Y. J. Feng and C. T. Chan, Relationship between surface dipole, work function and charge transfer: Some exceptions to an established rule, *Phys. Rev. B:Condens. Matter Mater. Phys.*, 2003, **68**(19), 195408, DOI: 10.1103/PhysRevB.68.195408.

79 A. Michaelides, P. Hu, M.-H. Lee, A. Alavi and D. A. King, Resolution of an Ancient Surface Science Anomaly: Work Function Change Induced by N Adsorption on W {100}, *Phys. Rev. Lett.*, 2003, **90**(24), 246103, DOI: 10.1103/PhysRevLett.90.246103.

80 A. Oprea, N. Bârsan and U. Weimar, Work function changes in gas sensitive materials: Fundamentals and applications, *Sens. Actuators, B*, 2009, **142**(2), 470–493, DOI: 10.1016/j.snb.2009.06.043.

81 P. C. Rusu, G. Giovannetti, C. Weijtens, R. Coehoorn and G. Brocks, First-principles study of the dipole layer formation at metal-organic interfaces, *Phys. Rev. B:Condens. Matter Mater. Phys.*, 2010, **81**(12), 125403, DOI: 10.1103/PhysRevB.81.125403.

82 Z. Saleem, S. S. Alarfaji, H. Shaheen, A. Majid and M. I. Khan, DFT investigation of pristine and li-functionalized TiS2 monolayers for toxic gas sensing applications, *J. Environ. Chem. Eng.*, 2025, **13**(5), 118534, DOI: 10.1016/j.jece.2025.118534.

83 M.-Q. Zhu, X.-F. Wang and P. Vasilopoulos, Transition metal-doped ZrS_2 monolayer as potential gas sensor for CO_2 , SO_2 , and NO_2 : density functional theory and non-equilibrium Green's functions' analysis, *J. Phys. D:Appl. Phys.*, 2025, **58**(13), 135306, DOI: 10.1088/1361-6463/adafb7.

84 H. Xu, L. Li, J. Xia, W. Zeng and Q. Zhou, Innovative doping strategies in ZrSe2: Co and Rh for enhanced agricultural greenhouse gas adsorption, *Surf. Interfaces*, 2025, **60**, 105988, DOI: 10.1016/j.surfin.2025.105988.

85 T. Zhang, G. He, Y. Gui, S. Liu, Y. Li and L. Cao, Investigating the adsorption performance of agricultural greenhouses hazardous gases on Rh doped HfX2 (X=S, Se) monolayers through DFT for potential gas sensor applications, *Surf. Interfaces*, 2024, **52**, 104914, DOI: 10.1016/j.surfin.2024.104914.